

図 11 非吸収面に対する非吸収形成率：(A) BMP-2 濃度 100µg/ml (B) BMP-2 濃度 400µg/ml ●：実験群, ▲：対照群。\*：p < 0.01

100µg/ml が 400µg/ml より有意に高かった ( $p < 0.01$ )。

8) TRAP 陽性細胞数

BMP-2 濃度 0µg/ml, 100µg/ml, 400µg/ml とともにすべての観察期間において実験群と対照群の間に有意差はみられなかった ( $p > 0.05$ ) (図 12)。

BMP-2 濃度での比較では、2 および 8 週で両群とも BMP-2 濃度 100µg/ml, 400µg/ml の間で有意差は

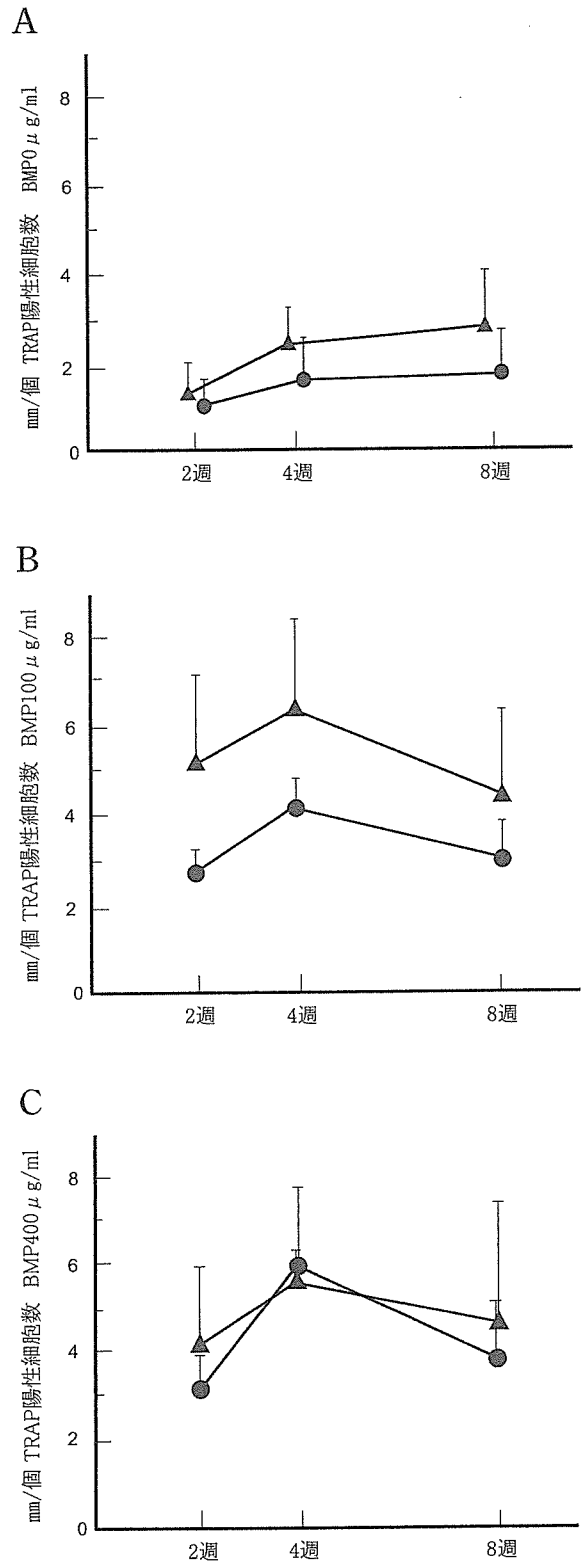


図 12 TRAP 陽性細胞数：(A) BMP-2 濃度 0µg/ml (B) BMP-2 濃度 100µg/ml (C) BMP-2 濃度 400µg/ml ●：実験群, ▲：対照群。\*：p < 0.01

みられなかった ( $p > 0.05$ )。4 週では実験群が BMP-2 濃度  $100\mu\text{g/ml}$  で  $4.0$  個/mm,  $400\mu\text{g/ml}$  で  $5.7$  個/mm であり, BMP-2 濃度  $400\mu\text{g/ml}$  が有意に高かった ( $p < 0.05$ )。対照群は BMP-2 濃度間で有意差はみられなかった ( $p > 0.05$ )。また, BMP-2 濃度  $0\mu\text{g/ml}$  と  $100$  および  $400\mu\text{g/ml}$  で比較すると, 対照群はすべての観察期間で BMP-2 濃度  $0\mu\text{g/ml}$  が  $100$  および  $400\mu\text{g/ml}$  に比較して有意に低かった ( $p < 0.01$ )。実験群は 2 週では有意差がみられなかったが ( $p > 0.05$ ), 4, 8 週では BMP-2 濃度  $0\mu\text{g/ml}$  が  $100$  および  $400\mu\text{g/ml}$  に比較して有意に低かった ( $p < 0.01$ )。

### 考 察

Hughes ら<sup>28)</sup>は, マウスの骨髓細胞を活性型ビタミン D 3 存在下で培養した後, ビスフォスフォネートを添加すると, ビスフォスフォネートの濃度依存的に TRAP 陽性細胞のアポトーシスを誘発し, 破骨細胞の機能を抑制することと, マウスにビスフォスフォネートを投与すると骨吸収が抑制され, 破骨細胞がアポトーシスしているのが観察されたと報告している。したがって本研究でも破骨細胞の機能を抑制するための方法としてビスフォスフォネート投与を行った。

Gong ら<sup>29)</sup>はラットを用いた実験においてビスフォスフォネートを  $1\mu\text{g/kg/day}$  濃度の腹腔内投与を行い, 破骨細胞の吸収活性が抑制されたことを報告しており, 本研究においても同様の濃度に設定した。さらにビスフォスフォネートの効果を確実に発揮させるために, 観察期間終了まで投与を継続した。本研究の結果, BMP-2 濃度  $0\mu\text{g/ml}$  でビスフォスフォネートを投与すると, 投与しなかった場合に比較して象牙質吸収は有意に少なかった。したがってビスフォスフォネートは破骨細胞様細胞の機能を十分に抑制していたと考えられた。一方でビスフォスフォネートを投与してもわずかな吸収は認められたので, 完全に破骨細胞様細胞の機能が停止していなかったと考えられた。

ビスフォスフォネートを投与しない対照群で, BMP-2 濃度  $400\mu\text{g/ml}$  が  $100\mu\text{g/ml}$  より穿下性の象牙質吸収が多くみられた。これは高濃度の BMP-2 で象牙質を処理した方が象牙質表面の吸収は穿下性であったとする Miyaji らの報告<sup>16)</sup>と一致していた。また, ビスフォスフォネートを用いた実験群の象牙質吸収率は, BMP-2 濃度が  $100\mu\text{g/ml}$ ,  $400\mu\text{g/ml}$  いずれの場合でも対照群に比較して有意に少なく 20% 以下まで抑制された。BMP-2 は破骨細胞の発現を活性化し, 破骨細胞前駆細胞に直接作用して破骨細胞の吸収

能を活性化させることが報告<sup>22)</sup>されている。したがってビスフォスフォネートは BMP-2 によって活性化された破骨細胞でも吸収機能を抑制することができ, さらに BMP-2 濃度に影響しないことが明らかになった。一方, TRAP 細胞数は実験群および対照群ともに同等の値であったことから, ビスフォスフォネートは破骨細胞の発現や分化を抑制するのではなく, 吸収機能を抑制したと考えられ, Murakami らの報告<sup>26)</sup>に一致していた。

本研究の結果, BMP-2 を塗布した象牙質表面におけるセメント質様硬組織形成は象牙質が一層吸収された後に硬組織が形成されているものと, 吸収されていない象牙質表面に硬組織が形成されているものが観察され, Miyaji ら<sup>15,16)</sup>天雲ら<sup>17)</sup>の報告に一致していた。総硬組織形成のうち BMP-2 濃度  $100\mu\text{g/ml}$  の対照群では非吸収面の硬組織形成は 20% 程度, 吸収面の硬組織形成は 80% 程度であり, BMP-2 濃度  $400\mu\text{g/ml}$  の対照群では非吸収面の硬組織形成は 30% 程度, 吸収面の硬組織形成は 70% 程度であったことから, BMP-2 処理した象牙質表面の硬組織形成には破骨細胞様細胞による象牙質面の吸収が大きく関与していることが示唆された。

BMP-2 は骨芽細胞を直接誘導することが報告<sup>1-5)</sup>されている。したがって本研究において非吸収面に形成されたセメント質様硬組織は, 破骨細胞様細胞の関与はなく, 象牙質に保持された BMP-2 が硬組織を直接誘導していると考えられた。また, 非吸収面に対する非吸収形成率はすべての観察期間で両群ともに同程度であったことから, ビスフォスフォネートは BMP-2 によるセメント質様硬組織の直接的な誘導には影響を及ぼさないことが明らかになった。しかし Suzuki ら<sup>30)</sup>は *in vitro* において, ビスフォスフォネートが骨芽細胞にも作用してアルカリフォスファターゼやチロシンフォスファターゼの活性に影響し, ビスフォスフォネートによる骨量減少抑制作用は骨芽細胞の活性化によるものもあることを示唆している。したがって *in vivo* におけるビスフォスフォネートの局所濃度などによっては, 骨芽細胞や硬組織形成に影響を及ぼす可能性も考えられる。

実験群 8 週の吸収面に対する吸収形成率は, 対照群より有意に少ない値だった。したがってビスフォスフォネート投与による破骨細胞様細胞の機能抑制によって, 硬組織形成が抑制されたと考えられた。破骨細胞様細胞によって象牙質吸収を受けた部位に硬組織が形成される機序として次の 2 つが考えられる。第一に, 骨のリモデリングと同様に破骨細胞が放出する因子が骨芽細胞前駆細胞の骨芽細胞への分化を促進した

と考えられる。第二に、象牙質基質には BMP などの成長因子が微量に含まれることが報告<sup>31,32)</sup>されており、Dallas ら<sup>20)</sup>は、破骨細胞による骨吸収によって骨基質中に埋め込まれた成長因子が放出され、これにより骨芽細胞が活性化されると報告していることから、象牙質基質が吸収された場合も同様に成長因子が放出されることで骨芽細胞が活性化して、硬組織が形成された可能性が考えられる。しかし BMP-2 濃度  $0\mu\text{g/ml}$  では吸収面に硬組織の形成はみられなかったため、象牙質基質内の成長因子はこの実験系では硬組織形成に関与せず、象牙質表面に塗布した BMP-2 がコラーゲンやアパタイトに保持され、これが破骨細胞様細胞による吸収によって放出された結果、硬組織が形成されたと考えられる。

本研究の結果、BMP-2 による象牙質表面のセメント質様硬組織形成は、吸収面に形成される硬組織が大部分を占めていることが明らかになり、さらにビスフォスフォネート投与によって破骨細胞様細胞の機能を抑制することで象牙質吸収面の硬組織形成が抑制されたことから、BMP-2 によるセメント質様硬組織形成は破骨細胞様細胞が重要な役割を有することが示唆された。

#### 謝 辞

本稿を終えるにあたり、本研究の遂行にご協力いただきました川村直人博士、天雲太一博士、大谷香織女史、得永佳介氏ならびに教室員各位に心より御礼申し上げます。

本論文の要旨は第 49 回秋季日本歯周病学会学術大会(2006 年 10 月 21 日)において発表した。なお、本論文は北海道大学審査学位論文である。

#### 文 献

- 1) Urist MR, Strate BS : Bone morphogenetic protein. *J Dent Res*, 50 : 1392-1406, 1971.
- 2) Wang EA, Rosen V, D'Alessandro JS : Recombinant human bone morphogenetic protein induces bone formation. *Proc Natl Acad Sci USA*, 87 : 2220-2224, 1990.
- 3) Tsuruga E, Takita H, Itoh H, Wakisaka Y, Kuboki Y : Pore size of porous hydroxyapatite as the cell-substratum controls BMP-induced osteogenesis. *J Biochem*, 121 : 317-324, 1997.
- 4) Isobe M, Yamazaki Y, Mori M, Ishikawa K, Nakabayashi N, Amagasa T : The role of human bone morphogenetic protein-2 in PLGA capsules at an extraskeletal site of the rat. *J Biomed Mater Res*, 45 : 36-41, 1999.
- 5) Okubo Y, Bessho K, Fujimura K, Konishi Y, Kusakoto K, Ogawa Y, Iizuka T : Osteoinduction by recombinant human bone morphogenetic protein-2 at intramuscular, subcutaneous and intrafatty sites. *Int J Oral Maxillofac Surg*, 29 : 62-66, 2000.
- 6) King GN, King N, Cruchley AT, Wozney JM, Hughes FJ : Recombinant human bone morphogenetic protein-2 promotes wound healing in rat periodontal fenestration defect. *J Dent Res*, 76 : 1460-1470, 1997.
- 7) Kinoshita A, Oda S, Takahashi K, Yokota S, Ishikawa I : Periodontal regeneration by application of recombinant human bone morphogenetic protein-2 to horizontal circumferential defects created by experimental periodontitis in beagle dogs. *J Periodontol*, 68 : 103-109, 1997.
- 8) Saito E, Saito A, Kawanami M : Favorable healing following space creation in rhBMP-2-induced periodontal regeneration of horizontal circumferential defects in dogs with experimental periodontitis. *J Periodontol*, 74 : 1808-1815, 2003.
- 9) 西村浩司, 小田島朝臣, 川浪雅光 : rhBMP-2 による歯周組織再生と骨性癒着抑制法の長期的観察. *日歯周誌*, 44 : 376-386, 2002.
- 10) 中根恒治, 松本敦至, 川浪雅光 : 中年齢ビーグル犬に rhBMP-2 を応用した場合の歯周組織再生. *日歯周誌*, 45 : 33-42, 2003.
- 11) 小田島朝臣, 本郷興人, 加藤 熙 : ポリ乳酸共重合体/ゼラチンスポンジ複合体を担体として用いた場合の rhBMP-2 によるセメント質と歯根膜および歯槽骨の誘導再生に関する研究. *日歯周誌*, 41 : 392-408, 1999.
- 12) Zaman K, Sugaya T, Kato H : Effect of recombinant human platelet-derived growth factor-BB and bone morphogenetic protein-2 application to demineralized dentin on early periodontal ligament cell response. *J Periodont Res*, 34 : 244-250, 1999.
- 13) 宮治裕史, 菅谷勉, 加藤 熙 : rhBMP-2 で処理した象牙質が歯肉線維芽細胞のアルカリ性フォスファターゼ活性と石灰化物形成に及ぼす効果. *日歯周誌*, 42 : 247-254, 2000.
- 14) 伊部敬介, 宮治裕史, 菅谷勉, 川浪雅光 : BMP-2 の歯根象牙質表面への塗布による歯周組織再生. *日歯周誌*, 46 : 278-287, 2004.
- 15) Miyaji H, Sugaya T, Miyamoto T, Kato K, Kato H : Hard tissue formation on dentin surfaces applied with recombinant human bone morphogenetic protein-2 in the connective tissue of the palate. *J Periodont Res*, 37 : 204-209, 2002.
- 16) Miyaji H, Sugaya T, Kato K, Kawamura N, Tsuji H, Kawanami M : Dentin resorption and cementum-like tissue formation by bone morphogenetic protein application. *J Periodont Res*, 41 : 311-315, 2006.

- 17) 天雲太一, 宮治裕史, 菅谷勉, 川浪雅光 : 象牙質表面処理剤の違いが BMP-2 による硬組織形成と象牙質吸収に及ぼす影響. 日歯周誌, 47 : 269-279, 2005.
- 18) Parfitt A.M : The mechanism of coupling: A role for the vasculature. *Bone*, 26 : 319-323, 2000.
- 19) Lener U.H : Bone remodeling in post-menopausal osteoporosis. *J Dent Res*, 85 : 584-595, 2006.
- 20) Dallas SL, Rosser JL, Mundy GR, Bonewald LF : Proteolysis of latent transforming growth factor- $\beta$  (TGF- $\beta$ )-binding protein-1 by osteoclasts. *J. Biol Chem*, 277 : 21352-21360, 2002.
- 21) Udagawa N, Itoh K, Li XT, Ozawa H, Takahashi N : Expression of osteoblast differentiation factor in mature osteoclasts. *J Bone Miner Res*, 17 : S344, 2002.
- 22) Kanatani M, Sugimoto T, Kaji H, Kobayashi T, Nishiyama K, Fukase M, Kumegawa M, Chihara K : Stimulatory effect of bone morphogenetic protein-2 on osteoclast-like cell formation and bone-resorbing activity. *J Bone Miner Res*, 10 : 1681-1690, 1995.
- 23) Kaneko H, Arakawa T, Mano H, Kaneda T, Ogasawara A, Nagasawa M, Toyama Y, Yabe Y, Kumegawa M, Hakeda Y : Direct stimulation of osteoclastic bone resorption by bone morphogenetic protein (BMP-2) and expression of BMP receptors in mature osteoclasts. *Bone*, 27 : 479-486, 2000.
- 24) Fleisch H, Russel R G G, Fransis M D : Bisphosphonate inhibit hydroxyapatite dissolution in vitro and bone resorption in tissue culture and in vivo. *Science*, 165 : 1262-1264, 1969.
- 25) Coxon P F, Helfrich H M, Robert V N, Said S, Ralston H S, Hamilton A, Rogers J M : Protein geranylgeranylation is required for osteoclast formation, function, and survival: inhibition by bisphosphonate and GGTI-298. *J Bone Miner Res*, 15 : 1467-1476, 2000.
- 26) Murakami H, Takahashi N, Sasaki T, Udagawa N, Tanaka S, Nakamura I, Zhang D, Barbier A, Suda T : A possible mechanism of the specific action of bisphosphonate on osteoclasts: tiludronate preferentially affects polarized osteoclasts having ruffled borders. *Bone*, 17 : 137-144, 1995.
- 27) Flanagan M A, Chambers J T : Inhibition of bone resorption by bisphosphonates: interactions between bisphosphonate, osteoclasts, and bone. *Calcif Tissue Int*, 49 : 407-415, 1991.
- 28) Hughes D, Wright K, Harry L UY, Sasaki A, Yoneda T, Roodman G, Mundy G, Boyce B : Bisphosphonate promote apoptosis in murine osteoclasts in vitro and in vivo. *J Bone Miner Res*, 10 : 1478-1487, 1995.
- 29) Gong L, Hoshi K, Ejiri S, Nakajima T, Shingaki S, Ozawa H : Bisphosphonate incadronate inhibits maturation of eptopic bone induced by recombinant human bone morphogenetic protein 2. *J Bone Miner Metab*, 21 : 5-11, 2003.
- 30) Suzuki K, Deyama Y, Nishikata M, Matsumoto A : The effects of bisphosphonates on tyrosine phosphatase activity of osteoblastic MC3T3-E1 cell. *Dentistry in Japan*, 37 : 35-38, 2001.
- 31) Bessho K, Tagawa T, Murata M : Purification of rabbit bone morphogenetic protein derived from bone, dentin, and wound tissue after tooth extraction. *J Oral Maxillofac Surg*, 48 : 162-169, 1990.
- 32) Finkelman R, Morhan S, Jennings J, Taylor A, Jepsen S, Baylink J : Quantitation of growth factors IGF- I , SGF/IGF- II , and TGF- $\beta$  in human dentin. *J Bone Miner Res*, 5 : 717-723, 1990.

## Electron gun using carbon-nanofiber field emitter

Y. Sakai, A. Haga, S. Sugita, S. Kita,<sup>a)</sup> S.-I. Tanaka,<sup>b)</sup> and F. Okuyama  
*Graduate School of Engineering, Nagoya Institute of Technology, Gokiso-cho, Showa-ku,  
 Nagoya 466-8555, Japan*

N. Kobayashi  
*Toshiba Corporation, 8 Shinsugita-cho, Isogo-ku, Yokohama 235-8523, Japan*

(Received 27 September 2006; accepted 9 December 2006; published online 30 January 2007)

An electron gun constructed using carbon-nanofiber (CNF) emitters and an electrostatic Einzel lens system has been characterized for the development of a high-resolution x-ray source. The CNFs used were grown on tungsten and palladium tips by plasma-enhanced chemical-vapor deposition. Electron beams with the energies of  $10 < E < 20$  keV were focused by the electrostatic lens and impinged on a W target for x-ray radiography. Analyzing the recorded x-ray radiographs, the focal spot size of the electron beam extracted from the CNFs was estimated to be  $D < 50$   $\mu\text{m}$  in diameter. Superior performance was realized by using CNFs with larger fiber radii (100–500 nm) grown sparsely on the metal tips, which were installed in a holder at the short length  $L=0.5$  mm. © 2007 American Institute of Physics. [DOI: 10.1063/1.2430650]

### I. INTRODUCTION

In recent years, carbon nanofibers<sup>1</sup> (CNFs) and carbon nanotubes<sup>2</sup> (CNTs) have been widely used as field electron emitters, due to their excellent physical and chemical properties, such as their small tip radius of curvature, high aspect ratio, mechanical toughness, and chemical stability. Although there is no strict classification between the CNTs and CNFs,<sup>3</sup> nanofibers with diameters ranging from 30 to 1000 nm are tentatively classified as CNFs. Since high-resolution transmission electron microscopy has revealed no parallel (001) fringes on the fiber sidewalls, our fibers might be more rod-like than tubular. Electrons extracted through field emission (FE) processes from the CNTs and CNFs have been successfully applied to x-ray sources.<sup>4–7</sup> X-ray radiography (XR) has been used over a broad area of medicine and industry. In XR, a small source size of x ray is required to obtain high-resolution images. Since field emission provides a narrower energy distribution of electrons and a smaller emission area, the field electron emitter is expected to be suitable for focusing electron beams into a small spot. Thus, the CNF and CNT emitter will make it possible to develop a high-resolution x-ray source operating in a nonultrahigh vacuum. To develop a high-resolution x-ray source using an electrostatic lens system, one has to fully understand the field emission and focusing characteristics of electron beams. Micro-focused x-ray tubes with CNT emitters have recently been reported.<sup>8,9</sup> Our previous study concerning the FE from CNFs grown on Pd wire indicates that CNFs with diameters larger than 100 nm provide intense and stable emission current.<sup>10</sup> In this study, field emission processes from the CNFs grown on etched metal (W and Pd) tips have been

extensively investigated, and focusing of electron beams with energies of  $10 < E < 20$  keV extracted from the CNFs was studied by inspecting x-ray radiographs.

### II. EXPERIMENT

The CNFs were grown on etched tungsten (W) and palladium (Pd) tips by the plasma-enhanced chemical vapor deposition (PECVD) method.<sup>11</sup> The metal tips were prepared by electrochemical etching of 0.5 mm diameter wires. The etching was performed in 1 mol KOH solution for W and in  $\text{H}_3\text{PO}_4$  solution for Pd. The W tips prepared in this way usually had radii of curvature of 1–2  $\mu\text{m}$ , while the Pd tips had radii of curvature of 3–20  $\mu\text{m}$  because of greater difficulty in the etching.

In the case of the W tips, after ultrasonic cleaning, a palladium (Pd) film serving as a catalyst of CNF growth was deposited on the tip by argon sputtering of a Pd disk. The film thickness was approximately 100 nm. CVD gases in the CNF growth were acetylene ( $\text{C}_2\text{H}_2$ ) at a pressure of 60 Pa and ammonia ( $\text{NH}_3$ ) at a pressure of 140 Pa. During CVD, the W tips were resistively heated, and the temperature of the substrates near the end of the tips was monitored with the aid of a radiation thermometer. By applying a negative dc voltage of 600 V to the heated tips for 20 min, CNFs could be synthesized on the tips. For the Pd tips, CNFs were grown directly on the tips in almost the same way as in W tips, but the CVD gas pressures were somewhat lower than those for W, i.e., 20 Pa for  $\text{C}_2\text{H}_2$  and 40 Pa for  $\text{NH}_3$ . The morphology of CNFs thus prepared was determined by scanning electron microscopy (SEM).

The experimental setup employed in the present study is schematically shown in Fig. 1. The vacuum chamber was pumped down to  $1.5 \times 10^{-7}$  Pa with both a turbo-molecular pump and an ion pump. By applying negative high voltage to the as-grown CNF emitter, FE electrons were extracted from the CNFs. In our measurements, no preheating of the CNF

<sup>a)</sup>Author to whom correspondence should be addressed; electronic mail: s.kita@nitech.ac.jp

<sup>b)</sup>Present address: Institute of Multidisciplinary Research for Advanced Materials, Tohoku University, 2-1-1 Katahira, Sendai 980-8577, Japan.

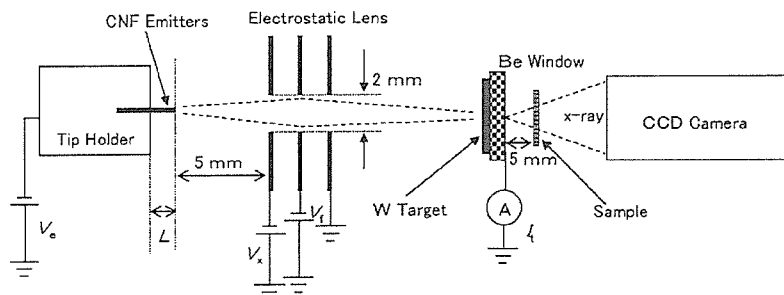


FIG. 1. Schematic drawing of apparatus used for characterization of electron beams extracted from CNF emitters.

emitter was attempted in order to remove the catalyst Pd particles. The electron beam extracted from the CNFs was accelerated to a desired energy of 10–20 keV and focused on the W-target by the electrostatic lens. Bombarding the W-film target (1  $\mu\text{m}$  in thickness) with the focused electron beam, x rays were made to radiate from the target. They passed through a beryllium (Be) window with a thickness of 200  $\mu\text{m}$  and escaped into the atmosphere. X-ray images of the samples were recorded by a charge-coupled device (CCD) camera, with a resolution of about 80  $\mu\text{m}/\text{pixel}$ . The electrostatic lens system consisted of three parallel electrodes. The first one in the lens was also used as an extractor electrode, the second one for focusing, and the third corresponded to an accelerated electrode. Each electrode was separated every 3 mm by ceramic spacers and was perforated in diameter 2 mm at the center. The W target was located at a position 10 cm apart from the CNF emitter, which was fixed in a metallic tip holder and placed 5 mm away from the extractor electrode. The distance  $L$  between the end of the tip and the holder indicated in Fig. 1 was varied, which allowed us to investigate the emission and focusing properties of electron beams as a function of  $L$ . In this study, the characteristics of field electron emissions from the CNFs were measured extensively, and the spot size of the focused electron beams was estimated by measuring the resolution of x-ray radiographs.

### III. RESULTS AND DISCUSSION

Figure 2 shows the SEM images of the CNF emitters used in this study. Figures 2(a) and 2(b) exhibit CNFs grown on etched W tips at the substrate temperatures of 400 and 800  $^{\circ}\text{C}$ , respectively. As seen in the figures, the CNFs were grown on the entire substrate surface and were well aligned, but their diameters depended on the substrate temperatures. As estimated from these images, the CNFs grown at 400 and 800  $^{\circ}\text{C}$  were 50–100 and 200–600 nm in diameter, respectively. Thus, the CNFs grown at higher temperatures on the W tips had larger diameters. Figure 2(c) shows the SEM images of CNFs grown around 700  $^{\circ}\text{C}$  on an etched Pd tip. Those CNFs had diameters of 50–1000 nm and were grown vertically from the substrate surface and sparsely distributed at the end of the Pd tip. These results may suggest that the sputter deposition of catalyst film leads to relatively uniform CNF growth. Since the catalyst nanoparticles were always observed at the top of CNFs, they presumably grew through the so-called tip-growth mechanism.<sup>1</sup>

The emission characteristics of the CNF emitters described above are exhibited in Fig. 3. Figure 3(a) shows the total emission current  $I$  measured as a function of the voltage  $V$  applied to the emitter. The measurements were performed for the tip lengths of  $L=3$  and 0.5 mm (see Fig. 1) without operating the electrostatic lens ( $V_f=0$  Fig. 1). In the figure, curves 1–3 are the data at  $L=3$  mm, and curves 1'–3' are those at  $L=0.5$  mm. Curves 1 and 1' correspond to the CNF emitter in Fig. 2(a), curves 2 and 2' to that in Fig. 2(b) and curves 3 and 3' to that in Fig. 2(c). The total emission cur-

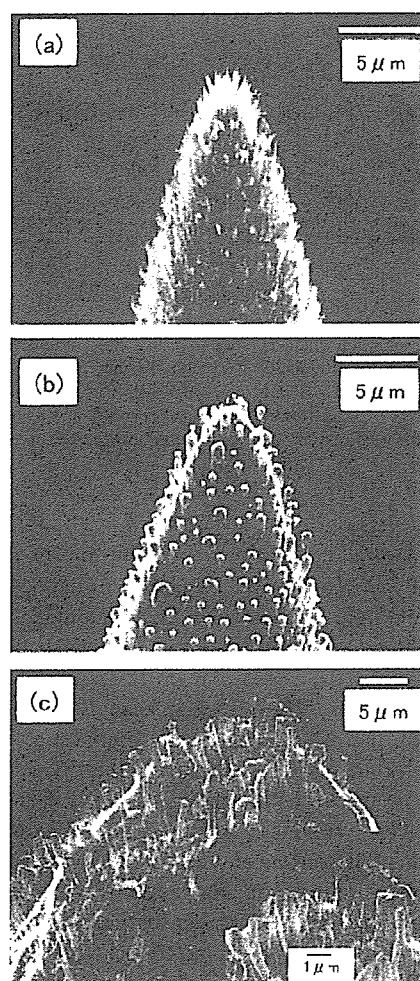


FIG. 2. SEM images of CNFs grown on metal tips. (a) CNFs on W tip at 400  $^{\circ}\text{C}$  (emitter 1). (b) on W tip at 800  $^{\circ}\text{C}$  (emitter 2). (c) CNFs on Pd tip (emitter 3). Inset shows image around top of emitter.

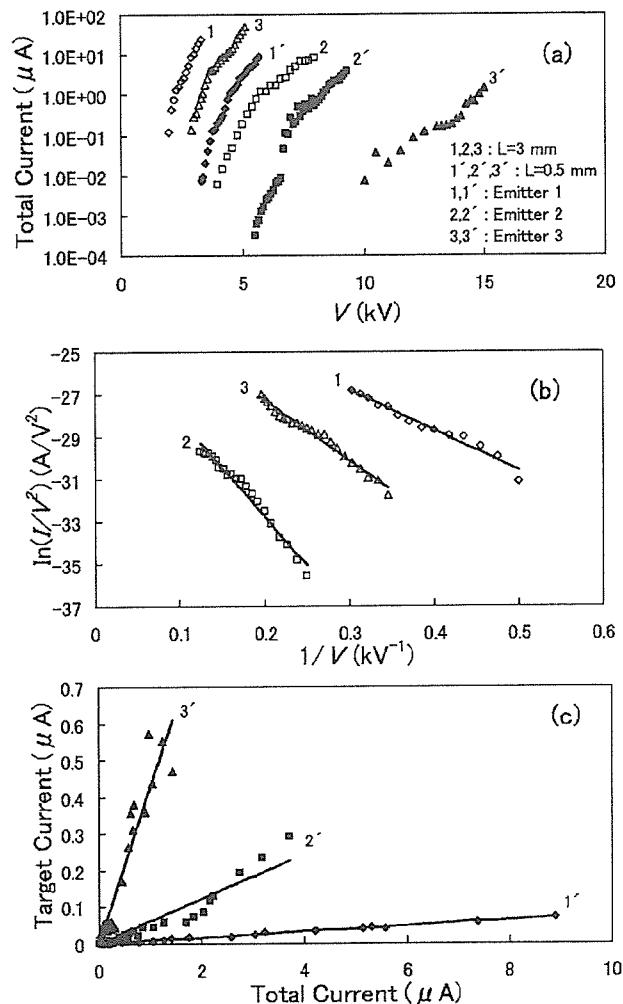


FIG. 3. Field emission characteristics of CNFs. (a) Current-voltage ( $I$ - $V$ ) curves measured for tip length  $L=3$  and  $0.5$  mm. Curves 1–3 are for  $L=3$  mm, and curves 1'–3' are for  $L=0.5$  mm. Curves 1 and 1' are for emitter 1, curves 2 and 2' for emitter 2, and curves 3 and 3' for emitter 3. (b) FN plots for total current, and (c) relation between target current  $I_t$  and total current  $I$ .

rent was measured up to  $50 \mu\text{A}$ . In all the curves, the current exponentially increased with elevations in the applied voltage  $V$ . As the figure makes clear, the magnitude of the field emission current strongly depends on the tip length  $L$ , and the voltages  $V$  for the  $L=0.5$  mm are 1.5–4 times higher than those for  $L=3$  mm. The  $L$  dependence is especially pronounced for the CNF emitter on the Pd tip. With any decrease in  $L$ , the electric field around the CNFs is strongly suppressed by the tip holder shown in Fig. 1. Hence, higher applied voltages are necessary to obtain certain emission currents. This  $L$  dependence of electric field strength is more effective in the emitter with a large radius of curvature  $R_0$  at the tip end, which might be the reason underlying the strong  $L$  dependence of the  $I$ - $V$  characteristics for the Pd tip in Fig. 3(a), the radius  $R_0$  of which was as large as  $14 \mu\text{m}$ . The  $L$  dependence could not be observed at  $L>1$  mm, but was strong at  $L<1$  mm. According to our simple estimation, this  $L$  dependence can be roughly presented by

$V \sim V_0[1 + A(R_0/L^4)]$  where  $V_0$  is voltage for a certain intensity at  $L>1$  mm, and the constant  $A$  is given by  $1.5 \times 10^{-8} \text{ m}^3$ .

Another remarkable fact about the experimental  $I$ - $V$  curves 1–3 is that the applied voltages  $V$  for the emitter on Pd (curve 3) with a radius of curvature of  $R_0=14 \mu\text{m}$  were appreciably lower than those for the W tip (curve 2) with a small radius of  $R_0=2 \mu\text{m}$ , possibly suggesting that the electric field depends not only on the  $R_0$  but also critically on the surface structure around the CNFs. Here we would like to focus our discussion on the experimental results at  $L=3$  mm, aside from the  $L$  dependence on the applied voltage  $V$  discussed above. An analysis using the well-known Fowler-Nordheim (FN) theory<sup>12</sup> provides valuable information on the local electric field on the CNFs surface. Figure 3(b) gives the FN plots [ $\ln(I/V^2)$  vs  $1/V$ ] evaluated from the experimental  $I$ - $V$  curves 1–3 in Fig. 3(a). Since all the plots lie along nearly straight lines, one can approximately evaluate the local electric field  $F$  on the CNFs from the slopes of these lines. According to our approximate calculations of the electric field around the substrate tip, which was assumed to have a semispherical structure with the radius  $R_0$  on a cylindrical shank, a macroscopic electric field  $E$  on the tip can be given by  $E \sim V/2R_0$  for the radius  $1 \leq R_0 \leq 20 \mu\text{m}$ .<sup>13</sup> Using the proportionality factor  $\beta$  giving field enhancement, the local field  $F$  on the CNFs is given by  $F = \beta E = \beta V/2R_0$ . Slope  $\alpha$  of the line in the FN plot is given by  $\alpha = 1.36 \times 10^7 R_0 \Phi^{3/2} / \beta$  [kV],<sup>12</sup> where  $\Phi$  denotes the work function of the CNFs, with  $R_0$  in meters. The theoretical and experimental values of  $\Phi$  reported so far for CNTs range from 4.2 to 5.1 eV.<sup>14–18</sup> This wide discrepancy might be due to differing respective evaluations of the CNT surface state. The FE electrons are considered to be emitted not only from the CNFs but also partly from the catalyst Pd on top of our CNFs. The work function of the Pd is approximately 5.1 eV.<sup>19</sup> Therefore, we may employ  $\Phi=5.0$  eV in our analysis, a value nearly common to both CNTs and Pd. By assuming a work function of  $\Phi=5.0$  eV, the enhancement factors are  $\beta \sim 14$  for emitter 1,  $\beta \sim 6$  for emitter 2, and  $\beta \sim 75$  for emitter 3. The local electric field largely depends on the growth density of CNFs; the electric field around a CNF in a densely populated area is strongly shielded by adjacent fibers.<sup>17</sup> This may be the reason why  $\beta$  varied from emitter to emitter. The  $\beta \sim 75$  for the Pd tip was much larger than those for W tips. The remarkably lower applied voltages in the  $I$ - $V$  curve 3 in Fig. 3(a) for the CNF emitter on the Pd tip is due to a larger enhancement factor of  $\beta \sim 75$ . As seen in the SEM images of Fig. 2, the CNFs on the Pd tip (emitter 3) have a lower density and a larger diameter size than those on the W tips (emitters 1 and 2). These findings should confirm the origin of the larger value of  $\beta$  ( $\sim 75$ ) for emitter 3.

To develop a fine-focusing x-ray source, one needs an electron beam with a higher brightness. The brightness is given by  $B = J/\Omega$ , where  $J$  and  $\Omega$  are electron density and a solid angle for the beam spread, respectively. Figure 3(c) shows the beam intensity  $I_t$  measured at the target located behind three electrodes for the lens system in Fig. 1. These are the results for the tip length of  $L=0.5$  mm. The ordinate in this figure indicates the beam intensity  $I_t$  and the abscissa

shows the total emission current  $I$ . The experimental results in Fig. 3(c) suggest that the beam intensity  $I_t$  is nearly proportional to the total current  $I$ , allowing one to immediately estimate the transmission rate of  $\gamma = dI_t/dI$  from the slope of these lines. The rates  $\gamma$  evaluated from the data in Fig. 3(c) were 0.008 for emitter 1 on W tip at 400 °C, 0.06 for emitter 2 on the W tip at 800 °C, and 0.35 for emitter 3 for the Pd tip. Thus, the transmission rate for CNF emitter 3 on the Pd tip was especially large, whereas the rate for emitter 3 measured at  $L=3$  mm was approximately  $\gamma=0.03$ , which was much smaller than the  $\gamma=0.35$  at  $L=0.5$  mm, confirming that the transmission rate  $\gamma$  can be appreciably enhanced by decreasing the tip length  $L$ . To interpret the experimental results, the FE patterns for emitter 3 have been observed using a phosphor screen installed in another ultrahigh vacuum chamber. According to the subsequent experiments, the angular spread of the FE electron for the tip length of  $L=0.5$  mm was 1/3 smaller than that for  $L=3$  mm. This is why the transmission rate for emitter 3 was appreciably increased by reducing the tip length  $L$ . These results for emitter 3 on the Pd tip indicate that the CNFs grown sparsely on the metal tip with a larger radius  $R_0$  provide a well-aligned electron beam. Since the spot size  $D$  of the focused electron beam strongly depends on the spread angle  $\Delta\theta$ ,  $D \propto (\Delta\theta)^3$ ,<sup>20</sup> the CNF emitter on the Pd tip might have a small spread angle  $\Delta\theta$ , and is expected to provide a focused beam of a smaller spot size and a higher resolution for x-ray radiography.

Using the spread half-angle  $\Delta\theta$ , beam intensity  $I$ , and effective emitting area  $S$ , the brightness  $B$  for the circular beam is written by  $B=I/\Omega=I/[\pi S(\Delta\theta)^2]$ . According to additional observations by a phosphor screen, FE patterns are composed of countable numbers of bright spots, and the distinguishable spots typically have spread half-angle of  $\Delta\theta \sim 60$  mrad, which is nearly the same as the previous observation.<sup>10</sup> Accordingly, one cannot directly determine the effective emitting area  $S$ . For an electron emitter composed of a single CNT, the effective emitting area  $S$  has been successfully evaluated using the FN formula.<sup>18</sup> In this study, as a trial evaluation, we have determined the  $S$  by analyzing the  $I$ - $V$  curves with the FN formula. The constant value  $A$  determining the magnitude of the ordinate  $\ln(I/V^2)$  in the FN plot [see Fig. 3(c)] is given by  $A=\ln(3.85 \times 10^{-7} \beta^2 S/\Phi R_0^2)$ . The spread angles  $\Delta\theta$  of the electron beams were estimated to be about 100 mrad for emitters 1 and 2, and 90 mrad for emitter 3, which will be discussed later. The brightness evaluated at the maximum applied voltage  $V$  is approximately given by  $7 \times 10^{11}$  A/(m<sup>2</sup> sr) for emitters 1 and 2, and  $8 \times 10^{12}$  A/(m<sup>2</sup> sr) for emitter 3, respectively. Thus, emitter 3 has the largest brightness  $B$  among the emitters characterized in this study, and is expected to give the best x-ray radiography performance. The brightness  $B=8 \times 10^{12}$  A/(m<sup>2</sup> sr) for emitter 3 gives the reduced brightness  $B_r=B/V=6 \times 10^8$  A/(m<sup>2</sup> sr V), which is somewhat lower than the values of  $B_r=(1.3-2.5) \times 10^9$  A/(m<sup>2</sup> sr V) reported in the early studies using CNTs.<sup>17</sup>

Luminescence on a phosphor screen originated by electron impact was first used to observe the focusing character of the electrostatic lens system. For this experiment, the W

target in Fig. 1 was replaced by the phosphor screen. The focusing voltage  $V_f$  applied to the second electrode in the lens system was approximately determined through the observation of luminescence on the screen. For the acceleration voltage of  $V_a=15$  kV ( $=-V_e$ ), the focusing voltage yielding the minimum spot size was  $V_f \sim -11$  kV ( $V_f/V_e \sim 0.73$ ), which was weakly dependent on the extraction voltage  $\Delta V = V_x - V_e$  (changed by the emitter). The optimal focusing voltage  $V_f$  was finally determined by observing the x-ray radiographs for each experimental condition of the emitter, the extraction voltage, and the accelerating voltage. The intensity of electron beams impinging on the W target was almost the same as those given in Fig. 3(c).

Figure 4 shows the x-ray images of a test chart composed of lead (Pb) lines with their line profiles measured to evaluate the spot size  $D$  in diameter of the focused electron beams. Under our experimental condition, electron spot size is considered to be nearly equal to the focal size of x-ray radiated from the W target. By taking x-ray images of the vertical and horizontal Pb lines, the spatial resolution of an x-ray source can be estimated. Figures 4(a) and 4(b) show the x-ray images for emitters 1 and 2 on the W tips, respectively. The exposure time for these images was 180 s. The width of the observed Pb line in Fig. 4(a) for emitter 1 was 62.5  $\mu\text{m}$ . The three stripes in the figure are sufficiently separated. The Pb linewidth in Fig. 4(b) for emitter 2 was 50  $\mu\text{m}$ , and the three stripes here are also well separated. As a result of those measurements, the spatial resolution on the x-ray images was estimated to be roughly 55 and 40  $\mu\text{m}$  for CNF emitters 1 and 2, respectively, on the W tips. Figure 4(c) also exhibits an x-ray image of Pb lines 50  $\mu\text{m}$  in width and its line profiles for emitter 3 on the Pd tip. The exposure time for this image was 300 s. As can be seen in the figure, the three stripes are quite well separated. By analyzing the blur structure of the Pb line edge in the x-ray image,<sup>21</sup> the spot sizes  $D$  for emitters 1, 2, and 3 were evaluated as approximately 60, 50, and 40  $\mu\text{m}$ , respectively. As the next step, the x-ray image of Fig. 4(c) was simulated by assuming the circular intensity distribution given by  $I=I_0 \exp(-1.7 \times 10^9 r^2)$ , where  $I_0$  is a proportionality constant, and  $r$  is the distance in meters with respect to the beam axis. As a result of the simulation, the spatial resolution on the x-ray image was evaluated as approximately 25  $\mu\text{m}$  for emitter 3. The performance of emitter 2 on the W tips was somewhat poorer than that of emitter 3. If emitter 2 was used with a smaller tip length than  $L=0.5$  mm, e.g.,  $L=0.25$  mm, better performance would result. Since the CNF emitter 3 on the Pd tip and emitter 2 on the W tip delivered superior performance, they may be used as an electron source for a high-resolution x-ray tube.

For further understanding of the focusing action by an electrostatic lens, focal-spot sizes for the used FE emitters have been simulated by employing a simple model program,<sup>13</sup> which calculates trajectories of FE electrons and makes for broadening of focal-spot size due to spherical aberration. The simulated results only weakly depend on the radius of curvature  $R_0$  at the tip end, and the focus-size diameter for the emitters used in this study is approximately given by  $D_{\text{th}}=0.054(\Delta\theta)^3$  m, where  $\Delta\theta$  is in units of radian. Connecting this calculated  $D_{\text{th}}$  and the experimental beam



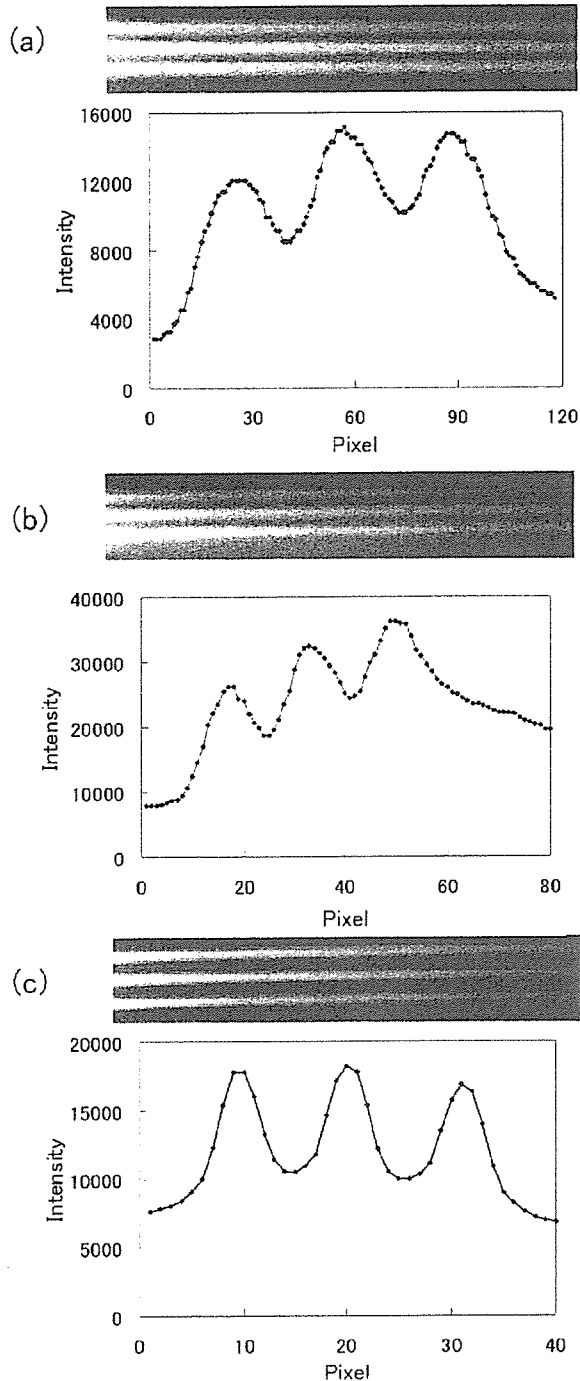


FIG. 4. X-ray images of test charts and their line profiles for electron beams extracted from CNF emitter at acceleration voltage of  $V_a=15$  kV. (a) For CNF emitter 1 on the W tip at 400 °C. Stripe width is 62.5  $\mu\text{m}$ . (b) For emitter 2 on W tip at 800 °C. Stripe width is 50  $\mu\text{m}$ . (c) For emitter 3 on Pd tip. Stripe width of test chart is 50  $\mu\text{m}$ .

sizes determined in this study ( $D=60$ , 50, and 40  $\mu\text{m}$  for emitters 1, 2, and 3, respectively), one can estimate the spread half-angle  $\Delta\theta$  of the electron beams. The results are  $\Delta\theta\sim 100$  mrad for emitters 1 and 2, and  $\Delta\theta\sim 90$  mrad for emitter 3. According to the trajectory analysis, the electrons entering the electrostatic lens with the angle  $\Delta\theta<200$  mrad can pass through the lens and reach the target. If one esti-

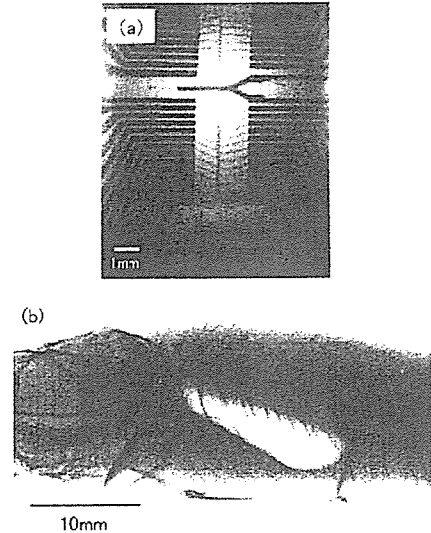


FIG. 5. Typical x-ray images taken with electron beam extracted from CNF emitter 3 on Pd tip. (a) LSI image ( $V_a=-15$  kV,  $T=300$  s), and (b) image of a small raw fish ( $V_a=13$  kV,  $T=450$  s).

mates focal size  $D^*$  using the maximum angle  $\Delta\theta=200$  mrad for the fully spread electron beam, one has  $D^*\sim 400$   $\mu\text{m}$ , which is much larger than the experimental sizes of  $D=40-60$   $\mu\text{m}$ . Thus, performance of the electron gun is significantly improved by using FE electrons with narrow angular spread. For further improvement of the focusing, however, it is desirable to fabricate the electron gun by employing an electrostatic Einzel lens composed of asymmetric electrodes.<sup>22</sup> According to our computer analysis, the asymmetric Einzel lens provides a focal-spot size smaller by a factor 1/10 than those for the lens obtained here.<sup>23</sup> The asymmetric Einzel lens has been very recently applied to a microfocused x-ray source with CNT emitter,<sup>24</sup> which has better resolution than that for symmetric lens.<sup>9</sup>

Figure 5 shows typical x-ray images demonstrating the performance maintained with the electron beam extracted from CNFs grown on the Pd tip. For the LSI image shown in Fig. 5(a), its interior structure, such as Cu wires ( $\sim 30$   $\mu\text{m}$  in width), could be readily observed nondestructively. The image of the small raw fish in Fig. 5(b) also sharply delineated such inner structures. X-ray images were also taken of the CNF emitter 2 on the W tip, and though not shown here, they are of nearly the same quality as those shown in Fig. 5. Thus, the images provided clear structural views of the biological as well as nonbiological materials. These results indicate that the CNF emitters grown on the etched metal tips can be successfully applied in the electron gun to develop a finely focused electron beam and a high-resolution x-ray source constructed with electrostatic and magnetic lenses.

Finally, we refer to the microfocused x-ray tubes using the CNT field emitter reported by other groups.<sup>8,9,24</sup> In their x-ray sources, electron emitters have been prepared in forms with a large diameter of 1–2 mm using CNT bundles, and provide intense electron emissions of around 1 mA, which is higher than the intensity in our electron gun. The x-ray spot sizes maintained in their sources are lower than 100  $\mu\text{m}$ , which is comparable to our results. From the standpoint of

the beam intensity, the larger size of emitters thus assures better performance, while an x-ray source with fine resolution (i.e., nanofocusing) will be realized by using a smaller CNT and/or CNF emitters with higher brightness.

#### IV. SUMMARY

We have synthesized CNFs on etched W tips at substrate temperatures of 400 and 800 °C, and on etched Pd wire at 700 °C by the PECVD method. For the W tips, the CNFs were grown vertically over the entire tip with diameters that were dependent on the substrate temperature. For the Pd tip, the CNFs were grown sparsely and their average diameters exceeded those for the W tips. The performance of CNF field emitters equipped in the electron gun has been extensively evaluated by repeated experiments. As for the field emission characteristics, CNF emitter 1 on the W tip and emitter 3 on the Pd-tip emitted electrons at lower voltages, while emitter 2 on the W-tip emitted electrons at somewhat higher voltages. Among the three emitters used in this study, the CNF emitter 3 on the Pd tip had the highest transmission rate. To investigate the focusing characteristics of the electron beams extracted from the CNF emitters we also recorded the x-ray radiographs using a CCD camera. From x-ray images of the x-ray test chart and their line profiles, we have confirmed that the CNF emitter on the W-tip grown at 800 °C and on the Pd tip at 700 °C have a focal spot size of less than 50  $\mu\text{m}$ . Better performance could be realized by using CNF emitters 2 and 3 with large fiber radii (100–500 nm) grown sparsely on the metal tips, which were installed in a holder at the short length  $L=0.5$  mm. These CNF emitters would be suitable for an electron gun of a high-resolution x-ray source equipped with electrostatic and magnetic lens systems.

#### ACKNOWLEDGMENTS

The authors gratefully acknowledge Dr. Y. Okazaki, Y. Matsumoto, R. Kubota, and Y. Oga (Nagoya Institute of Technology, Nagoya, Japan) for their considerable contributions to this work. They are also greatly indebted to Professor O. Eryu (Nagoya Institute of Technology, Nagoya, Japan) for preparation of the W film target in XR. They would

also like to thank Dr. S. Senda (Nagoya Institute of Technology, Nagoya, Japan), Dr. A. Yamaguchi, Dr. N. Aoki (Toshiba Corporation, Yokohama, Japan), and Professor M. Miyoshi (The University of Tokyo, Tokyo, Japan) for their valuable discussions. This study was financially supported by SENTAN, JST.

- <sup>1</sup>A. Oberlin, M. Endo, and T. Koyama, *J. Cryst. Growth* **32**, 335 (1976).
- <sup>2</sup>S. Iijima, *Nature (London)* **354**, 56 (1991).
- <sup>3</sup>A. V. Melechko, V. I. Merkulov, T. E. McKnight, M. A. Guillom, K. L. Klein, D. H. Lowndes, and M. L. Simpson, *J. Appl. Phys.* **97**, 041301 (2005).
- <sup>4</sup>H. Sugie, M. Tanemura, V. Filip, K. Iwata, K. Takahashi, and F. Okuyama, *Appl. Phys. Lett.* **78**, 2578 (2001).
- <sup>5</sup>G. Y. Yue, Q. Qiu, B. Gao, Y. Chang, J. Zhang, H. Shimoda, S. Chang, J. P. Lu, and O. Zhou, *Appl. Phys. Lett.* **81**, 355 (2002).
- <sup>6</sup>T. Matsumoto and H. Mimura, *Appl. Phys. Lett.* **82**, 1637 (2003).
- <sup>7</sup>S. Senda, Y. Sakai, Y. Mizuta, S. Kita, and F. Okuyama, *Appl. Phys. Lett.* **85**, 5679 (2004).
- <sup>8</sup>K. Kawakita, K. Hata, and H. Sato, *J. Vac. Sci. Technol. B* **24**, 950 (2006).
- <sup>9</sup>Z. Liu, J. Zhang, G. Yang, Y. Cheng, O. Zhou, and J. Lu, *Rev. Sci. Instrum.* **77**, 054302 (2006).
- <sup>10</sup>S. Kita, Y. Sakai, T. Fukushima, Y. Mizuta, A. Ogawa, S. Senda, and F. Okuyama, *Appl. Phys. Lett.* **85**, 4478 (2004).
- <sup>11</sup>M. Tanemura, K. Iwata, K. Takahashi, Y. Fujimoto, F. Okuyama, H. Sugie and V. Filip, *J. Appl. Phys.* **90**, 1529 (2001).
- <sup>12</sup>R. H. Fowler and L. W. Nordheim, *Proc. R. Soc. London, Ser. A* **119**, 103 (1928).
- <sup>13</sup>R. Kubota, A. Haga, J. Kawashima, and S. Kita (unpublished).
- <sup>14</sup>S. Suzuki, C. Bower, Y. Watanabe, and O. Zhou, *Appl. Phys. Lett.* **76**, 4007 (2000).
- <sup>15</sup>J. Zhao, J. Han, and J. P. Lu, *Phys. Rev. B* **65**, 193401 (2002).
- <sup>16</sup>W. Y. Li, K. Goto, J. Takioto, S. Tanaka, H. Morikawa, and R. Shimizu, *J. Surf. Anal.* **11**, 170 (2004).
- <sup>17</sup>N. de Jonge and J. M. Bonard, *Philos. Trans. R. Soc. London, Ser. A* **362**, 2239 (2004).
- <sup>18</sup>N. de Jonge, M. Allieux, M. Doytcheva, M. Kaiser, K. B. K. Teo, R. G. Lacerda, and W. I. Milne, *Appl. Phys. Lett.* **85**, 1607 (2004).
- <sup>19</sup>H. B. Michaelson, *J. Appl. Phys.* **48**, 4729 (1977).
- <sup>20</sup>P. J. Grundy and G. A. Jones, in *Electron Microscopy in the Study of Materials*, edited by B. R. Coles (Edward Arnold, London, 1976).
- <sup>21</sup>S. Senda, M. Tanemura, Y. Sakai, Y. Ichikawa, S. Kita, T. Otsuka, A. Haga, and F. Okuyama, *Rev. Sci. Instrum.* **75**, 1366 (2004).
- <sup>22</sup>G. H. N. Riddle, *J. Vac. Sci. Technol.* **15**, 857 (1978).
- <sup>23</sup>A. Yamaguchi, M. Miyoshi, A. Haga, J. Kawashima, Y. Oga, and S. Kita (unpublished).
- <sup>24</sup>Z. Liu, G. Yang, Y. Z. Lee, D. Bordelon, J. Lu, and O. Zhou, *Appl. Phys. Lett.* **89**, 103111 (2006).

# Low temperature synthesis of hydroxyapatite from $\text{CaHPO}_4 \cdot 2\text{H}_2\text{O}$ and $\text{Ca}(\text{OH})_2$ based on effect of the spark plasma system (SPS)

Mamoru Omori<sup>a,\*</sup>, Takamasa Onoki<sup>a</sup>, Toshiyuki Hashida<sup>a</sup>,  
Akira Okubo<sup>b</sup>, Yoshihiro Murakami<sup>b</sup>

<sup>a</sup> Graduate School of Engineering, Tohoku University, Fracture and Reliability Research Institute,  
6-6-11 Aoba, Aramaki, Aoba-ku, Sendai 980-8579, Japan

<sup>b</sup> Institute for Materials Research, Tohoku University, 2-1-1 Katahira, Aoba-ku, Sendai 980-8577, Japan

Received 28 November 2004; received in revised form 8 December 2004; accepted 23 April 2005

Available online 29 June 2005

## Abstract

A mixture of 6 mol of  $\text{CaHPO}_4 \cdot 2\text{H}_2\text{O}$  and 4 mol of  $\text{Ca}(\text{OH})_2$  was reacted to produce hydroxyapatite (HA) by spark plasma system (SPS). The reaction was carried out at 300–1200 °C under pressure of 20–670 MPa for 10 min in a vacuum. HA formation started at 300 °C at 600 MPa and was completed at 500 °C at 670 MPa, the same product being obtained at 1200 °C in air using a furnace. The temperature of the HA formation increased with decreasing pressure and was 1150 °C under 20 MPa. There was a linear relationship between the reaction temperature and pressure. The crystal size of the HA prepared at 500 °C at 670 MPa and that at 600 °C at 600 MPa by SPS were less than 1 and 2 μm, respectively.

© 2005 Elsevier Ltd and Techna Group S.r.l. All rights reserved.

**Keywords:** Hydroxyapatite; Hydroxyapatite synthesis; Spark plasma system (SPS); Spark plasma sintering (SPS); Calcium phosphate

## 1. Introduction

Powder sintering has been based on sintering at atmospheric pressure or sintering under high pressure. Although these techniques have enabled the manufacture of various kinds of useful products from metal and ceramics, their limited effectiveness for the production of advanced materials has recently become apparent. The spark plasma system (SPS) was developed for sintering metal and ceramic powders in plasma as well as in an electric field [1]. SPS is characterized by a pulsed direct electric current, which is similar to that of an electric discharge machine. Unique products which cannot be made by ordinary methods have been created from ceramics, metals and polymers by SPS [2]. The formation of these products is based on the effect of the pulsed electric field, where spark plasma is generated between powders and a skin current can run on particle

surface. The spark plasma activates some chemical bonds, and crystal growth is enhanced by the skin current [2]. The mobility of dislocations is accelerated in the pulsed direct electric field [3].

Hydroxyapatite (HA,  $\text{Ca}_{10}(\text{PO}_4)_6(\text{OH})_2$ ) is one of the most bioactive ceramics [4]. The chemical composition of HA consists of OH groups which are eliminated at high temperature. The stability of HA depends on the partial pressure of  $\text{H}_2\text{O}$  [5]. The HA powder can be stably sintered at 1300 °C in air using a furnace [6]. On the other hand, HA is stable below 1050 °C in a vacuum [7]. The decomposition temperature of HA is lowered till 800 °C by the catalytic action of Ti [8,9]. The majority of HA syntheses are carried out under the influence of water as follows: (1) precipitation method [10,11]; (2) hydrolysis method [12]; (3) hydrothermal method [13,14]; and (4) hydrothermal hot-pressing method [15]. HA is synthesized from 6 mol of  $\text{CaHPO}_4$  (DCP) and 4 mol of  $\text{Ca}(\text{OH})_2$  (CHO) without water by solid state reaction [4], although the synthetic condition has not been clarified.

\* Corresponding author. Tel.: +81 22 217 7524; fax: +81 22 217 4311.  
E-mail address: m-omori@rift.mech.tohoku.ac.jp (M. Omori).

In this study, 6 mol of  $\text{CaHPO}_4 \cdot 2\text{H}_2\text{O}$  (DCPD) and 4 mol of CHO were reacted to produce hydroxyapatite by SPS. The reaction was carried out at 300–1200 °C under pressure of 20–670 MPa. The HA formation was investigated by X-ray diffractometry, and the grain size of the prepared HA was observed by scanning electron microscopy (SEM) and transmission electron microscopy (TEM).

## 2. Experimental

### 2.1. Materials and reaction

The starting powders were DCPD and CHO (Wako Pure Chemical Ind., Japan, reagent grade), 6 mol of DCPD and 4 mol of CHO being mixed with an agate mortar and pestled for 20 min. These two materials were reacted by SPS (Sumitomo Coal Mining Co. Ltd., Japan, SPS1050). The mixed powder was put in a graphite die or a hard metal die and heated from 300 to 1200 °C at 20–670 MPa in a vacuum. The heating rate was controlled toward the goal temperature of 1000 °C as follows: from 20 to 900 °C at 100 °C/min, from 900 to 980 °C at 20 °C/min and from 980 to 1000 °C at 5 °C/min. The holding time at the goal temperatures was 10 min. For comparison with the SPS sample, the mixed powder was reacted from 500 to 1200 °C in air in a furnace without using SPS.

### 2.2. Decomposition of materials and characterization of the reacted product

The decomposition temperature of DCPD was determined by differential scanning calorimetry at a heating rate of 0.67 °C/s in air (Seiko Instruments, Japan, SII DSC 6300). The reacted products were subjected to X-ray diffraction (XRD) by an X-ray diffractometer (Rigaku, Japan, Rotaflex, RU-200B) using the  $\text{Cu K}\alpha$  line. The surface of the reacted product was polished to make a mirror surface and was etched at 1000 °C for 30 min in air. The etched surface of the sintered product was observed by a scanning electron microscope (SEM) (JEOL, Japan, JXA-8621MX, and Hitachi, Japan, S-800). The microstructure was analyzed by a transmission electron microscope (TEM) (JEOL, Japan, JT-007).

## 3. Results

### 3.1. Reaction in furnace

The results of the DSC measurement indicated that DCPD lost water and was transformed into DCP at 149 °C. DCP was decomposed at 460 °C. It was confirmed by X-ray diffractometry that CHO was stable until 900 °C and then decomposed into CaO over 1000 °C. The mixture of 6 mol of DCP and 4 mol of CHO was reacted in air in a furnace, not

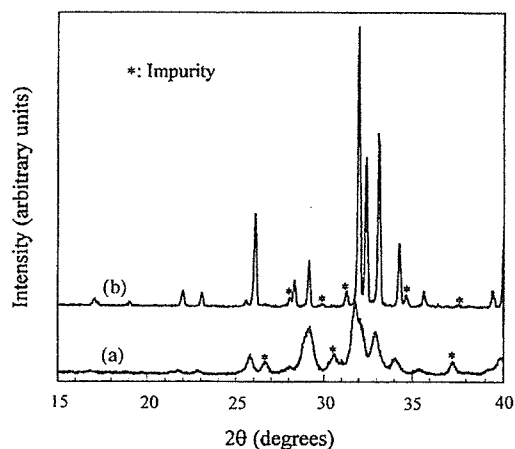


Fig. 1. XRD patterns of the products reacted in furnace for 1 h in air: (a) at 600 °C and (b) at 1200 °C.

using SPS. The reaction of DCPD and CHO did not occur at 500 °C, but started near 600 °C. Fig. 1a shows that HA with impurities was formed at 600 °C for 1 h. The diffraction peaks of the product was not sharp and exhibited the formation of a small crystallite, i.e. nucleus. This nucleus was unstable at this temperature and disappeared after heating at 600 °C for 10 h. The nucleus did not grow to stable size at 600 °C in the furnace.

The formation of HA from DCP and CHO was indistinct below 1000 °C, but was distinguishable at 1200 °C. The reacted product consisted of HA and a small amount of the impurity which was not identified, as shown in Fig. 1b. It was clear that preparation of HA was possible in air by solid state reaction. Judging from the half-value width of the diffraction peaks, the crystal of the product which prepared at 1200 °C was not a nucleus, The HA crystal was stable and did not decompose after the reaction at 1200 °C for 10 h in air. The impurity neither decreased nor increased after the long reaction.

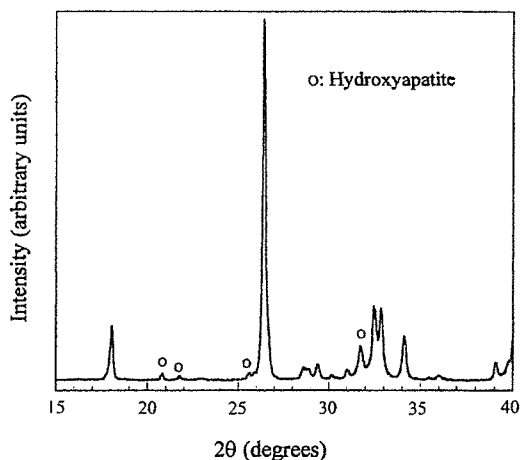


Fig. 2. XRD pattern of the product reacted at 300 °C at 600 MPa for 10 min by SPS.

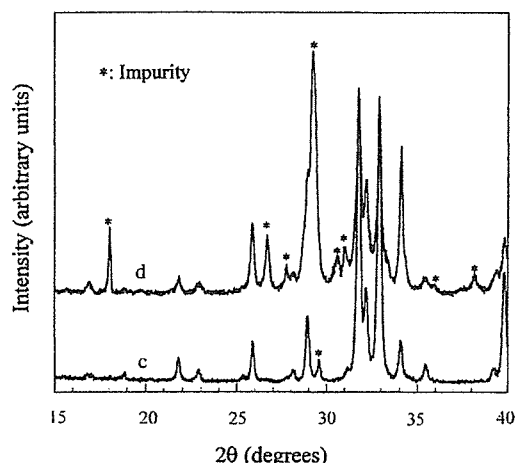


Fig. 3. XRD patterns of the products reacted at 500 °C for 10 min by SPS: (c) at 670 MPa and (d) at 20 MPa.

### 3.2. Reaction by SPS

The reaction by SPS was different from that conducted in air using a furnace. The X-ray diffraction pattern shown in Fig. 2 suggests that DCP and CHO started reacting at 300 °C under high pressures. This reaction occurred at 600 MPa, but it was not completed within 1 h. The low pressure of 20 MPa did not induce the reaction between these two compounds. The HA formation was clear for the product reacted at 500 °C at 670 MPa for 10 min. This product was composed of HA and a small amount of impurities, as shown in Fig. 3c. The impurities were not identified. The X-ray diffraction pattern shown in Fig. 3d indicates that the impurities increased at 20 MPa. SPS enabled production of HA at 500 °C, despite under the high pressure. The HA formation temperature increased with decreasing pressure.

Fig. 4e shows that the product reacted at 600 °C at 600 MPa was the nearly same as that prepared at 500 °C. The impurity was not removed after the reaction at 500 and

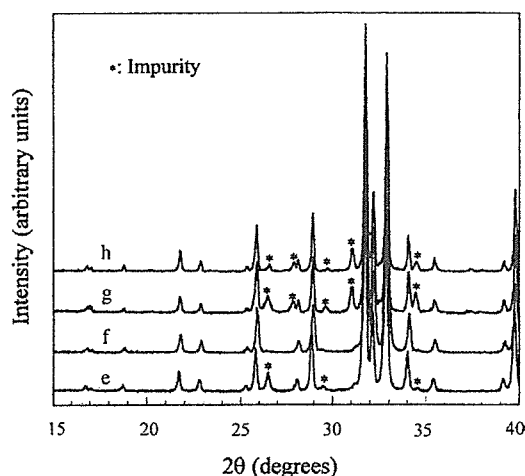


Fig. 4. XRD patterns of the products reacted for 10 min by SPS: (e) at 600 °C at 600 MPa; (f) at 700 °C at 480 MPa; (g) at 1000 °C at 120 MPa and (h) at 1150 °C at 20 MPa.

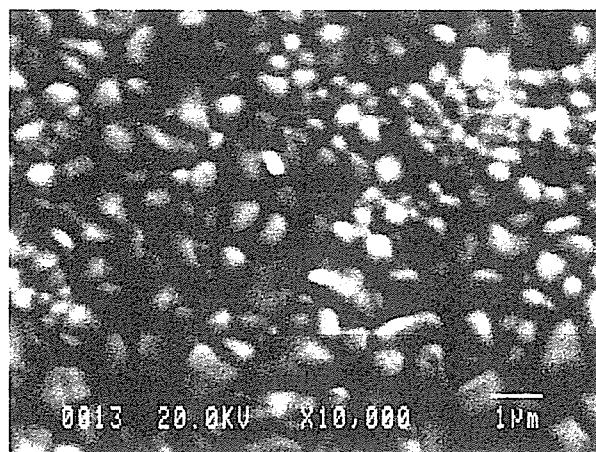


Fig. 5. SEM image of the product reacted at 500 °C at 670 MPa for 10 min by SPS.

600 °C for 1 h and persisted in the product. A pure HA product was obtained by the reaction at 700 °C at 470 MPa for 10 min, as shown in Fig. 4f. The crystals of those products were stable and different from the nucleus synthesized at 600 °C in the furnace. HA was prepared at 1000 °C at 120 MPa and at 1150 °C at 20 MPa. X-ray diffraction pattern of the products reacted at these two temperatures is shown in Fig. 4g and h. The reacted product contained unidentified impurities. The impurities remained in the product reacted at 1200 °C at 20 MPa.

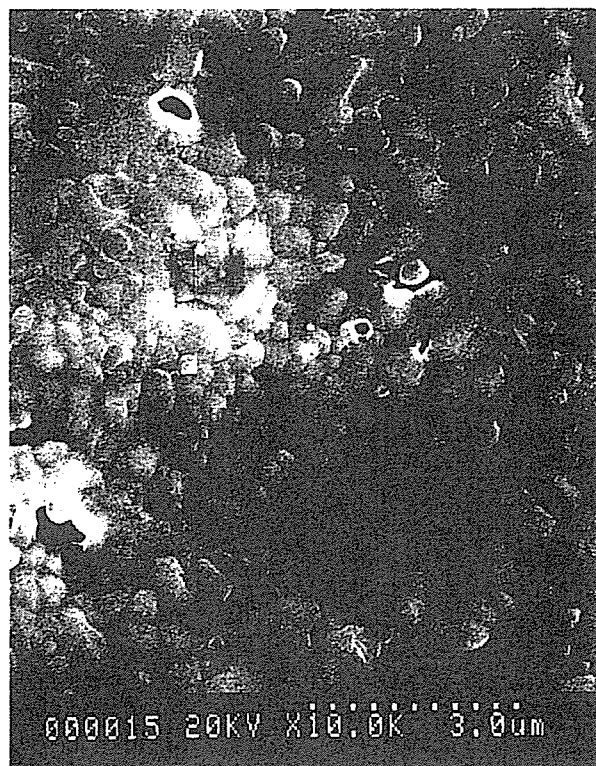


Fig. 6. SEM image of the product reacted at 600 °C at 600 MPa for 10 min by SPS.

The diffraction peaks were broadened in the products reacted at 500 °C compared with those of the products prepared at 1200 °C in the furnace and from 600 to 1150 °C by SPS. This broadening suggested that the crystal size of the product was small or that the crystallinity was not good.

The crystal size was measured on the etched surface of the product reacted at 500 °C at 670 MPa for 10 min. The SEM image shown in Fig. 5 indicates the crystal size to be less than 1  $\mu\text{m}$ . Fig. 6 shows that the crystal size of the product reacted at 600 °C at 600 MPa was less than 2  $\mu\text{m}$ . TEM observation of the HA crystal reacted at 1150 °C at 20 MPa for 10 min revealed its size to be less than 2  $\mu\text{m}$ . The crystal size of the products reacted from 500 to 1150 °C was not greatly affected by the reaction temperature.

#### 4. Discussion

DCPD lost water of crystallization at 149 °C and became to DCP. The real reaction of DCPD and CHO is that of DCP and CHO over this temperature. The reaction of these two compounds starts at 600 °C in the furnace after decomposition of DCP, and HA nuclei with impurities are produced. The nucleus is unstable and decomposed without water. Time is required for the nucleus to change into a stable crystal at the low temperature when using the furnace. The water supply based on the decomposition of the two compounds cannot last for a long time, and the nucleus is transformed into other stable compounds different from HA. The product reacted at 1200 °C for 1 h in the furnace contained the impurity, and its amount did not increase nor decrease by the long reaction for 10 h. This impurity is not derived from decomposition of the formed HA because  $\beta\text{-Ca}_3(\text{PO}_4)_2$  is not included, but it is produced in the course of the reaction of DCP and CHO.

The Ca/P ratio of hydroxyapatite is not constant and varies from 1.65 to 1.72 [16]. The product fabricated from the mixture of 6 mol of DCPD and 4 mol of CHO must result in the composition of 1.67, and the one reacted at 700 °C at 480 MPa corresponds it not accompanied by the impurity. The impurity in other products suggests that the composition of the product differs from that of the mixture. There was an impurity peak at  $2\theta = 29.6^\circ$  in the XRD pattern shown in Fig. 3c. The mixture was synthesized from 3.9 to 4.1 mol of CHO for 6 mol of DCPD and reacted at 500 °C at 670 MPa to eliminate this impurity. The XRD patterns shown in Fig. 7i and j, which were obtained from the inside and surface of the same product pellet, were due to the product synthesized from 6 mol of DCPD and 3.93 mol of CHO (Ca/P = 1.66). The intensity of the impurity peaks was the least among the products reacted in that composition variation. As shown in Fig. 7i, that impurity peak at  $2\theta = 26.9^\circ$  was removed, and new weak ones appeared at  $2\theta = 20.4^\circ$ ,  $26.6^\circ$ ,  $31.2^\circ$  and  $34.5^\circ$ . The feature of the impurity peaks indicated in Fig. 7j was not same as that of the inside and revealed that the Ca/P ratio varied from the surface to the inside. The

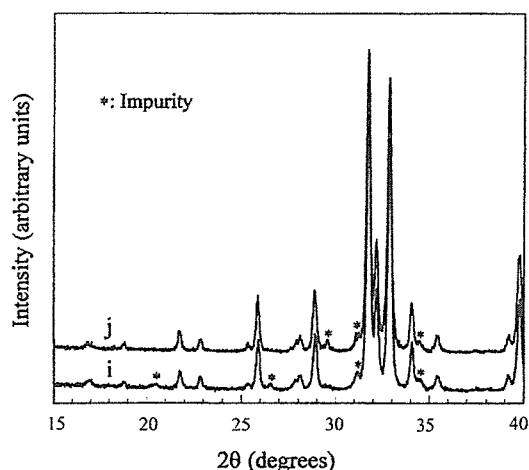


Fig. 7. XRD patterns of the products reacted from 6 mol of DCPD and 3.93 mol of CHO at 500 °C at 670 MPa for 10 min by SPS and measured: (i) at the inside and (j) at the surface.

impurity does not mean that the reaction is not completed at each temperature and pressure.

SPS can enhance the reaction of DCP and CHO, and HA is produced at lower temperatures under higher pressures. The reaction by SPS is different from that in the furnace. DCP was not damaged at 20 and 670 MPa at 300 °C by SPS. On the other hand, CHO was slightly decomposed at 20 and 670 MPa at 300 °C. The reaction of DCP and CHO is initiated at 300 °C by degradation of CHO. High pressure enhances the reaction, and HA is formed at 500 °C under the pressure of 670 MPa, which is near the endurance limit of hard metal. The product reacted at 500, 600, 1000 and 1150 °C consists of HA and small portions of impurities, and they comes from the excess DCP or CHO. There is a liner relationship between the reaction temperature and pressure, as shown in Fig. 8. The high pressure causes the isolated particles to come into tight contact. Furthermore, since mobility of dislocations is enhanced in the pulsed electric field [3], it is possible that the compound particles are plastically deformed at lower temperatures. The contact area (or necking area) is effectively widened under high pressure by plastic deformation. The

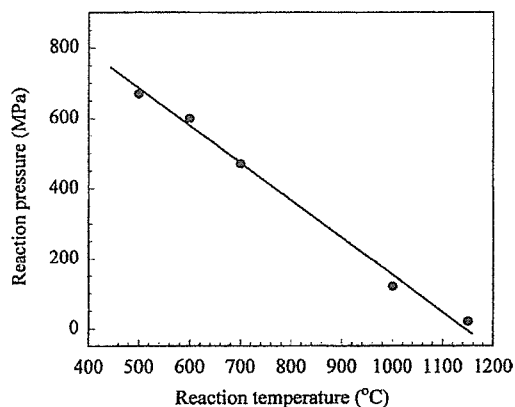


Fig. 8. Temperature vs. pressure for HA formation by SPS.

molecules of the two compounds can diffuse through the wide contact area.

One of the SPS effects is based on the skin current, which appears on the surface of particles in the pulsed electric field and results in acceleration of crystal growth [2]. If the skin current is determined by the voltage applied to the graphite die, its density varies with the free surface of particles excluding the contact area. The volume of the free surface decreases at high pressure because of the increased contact area. The migration of Al atoms in the Al film is accelerated through direct current [17], but there is no evidence regarding the accelerated migration of molecules in the pulsed direct electric field. The skin current may carry the DCP and CHO molecules on the surface of the particles. The wide contact area and the enhanced migration enable the reaction at the low temperatures and result in the linear relationship between the reaction temperature and pressure.

The half-value width of the X-ray diffraction peak suggests that the crystal size of the product reacted at 500 °C is less than that of the ones synthesized from 600 to 1150 °C. However, the size observed by SEM and TEM is almost same, i.e. less than 1 and 2 μm. The crystals prepared at 500 °C contain many of crystal imperfections, such as lattice defects and stacking faults, and the diffraction peaks are broadened by them. The crystal size of the products reacted at 600 and 1150 °C is not different. This result is contrary to the fact that growth rate of crystal is faster at higher temperature. HA molecules can be carried on the surface of the HA crystal under higher pressures by the dense skin current, and the crystal growth is promoted by it.

## 5. Conclusion

$\text{CaHPO}_4 \cdot 2\text{H}_2\text{O}$  (6 mol) and  $\text{Ca}(\text{OH})_2$  (4 mol) were reacted at 1200 °C for 1 h in air using a furnace and produced HA. Using the spark plasma system, HA formation started at 300 °C at 600 MPa and was completed at 500 °C at 670 MPa for 10 min. The temperature of the HA formation increased with decreasing pressure. HA was prepared for 10 min at 600 °C, 700, 1000 and 1150 °C under pressures of 600, 470, 120 and 20 MPa, respectively. There was a linear relationship between the temperature and pressure of the SPS reaction. The effects of SPS, namely, the plastic deformation enhanced in the pulsed electric field and the skin current generated on particle surface in an electric field, enabled the reaction of the two compounds at lower temperatures under higher pressures. The size of the HA crystal reacted at 500 °C at 670 MPa was similar to that of the one formed at 1150 °C at 20 MPa. The skin current under

the high pressure was responsible for the crystal growth of HA at the low temperatures.

## Acknowledgements

This study was supported by Research on Advanced Medical Technology in Health and Labour Sciences Research Grants from the Ministry of Health, Labour and Welfare of Japan. The authors are thankful to Mr. Shun Ito (Institute for Materials Research, Tohoku University) for transmission electron microscope, observations.

## References

- [1] K. Inoue, Electric-discharge sintering. US Patent No. 3,241,956 (1966).
- [2] M. Omori, Sintering, consolidation, reaction and crystal growth by the spark plasma system (SPS), *Mater. Sci. Eng. A287* (2000) 183–188.
- [3] H. Conrad, Electroplasticity in metals and ceramics, *Mater. Sci. Eng. A287* (2000) 276–287.
- [4] R.Z. Legeros, J.P. Legeros, Dense hydroxyapatite, in: L.L. Hench, J. Wilson (Eds.), *Advanced Series in Ceramics: Introduction to Bioceramics*, vol. 1, World Scientific, NJ, USA, 1991, pp. 139–180.
- [5] P.V. Ribound, Comparaison de la stabilité de l'apatite d'oxyde de fer et de l'hydroxyapatite a haute temperature, *Bull. Soc. Chim. Fr.* (1968) 1701–1703.
- [6] P. Van Landuyt, F. Li, J.P. Keustermans, J.M. Streydio, F. Delannay, E. Munting, The influence of high sintering temperatures on the mechanical properties of hydroxyapatite, *J. Mater. Sci.: Mater. Med.* 6 (1995) 8–13.
- [7] J.C. Trombe, G. Montel, Some features of the incorporation of oxygen in different oxidation states in the apatitic lattice. I. On the existence of calcium and strontium oxyapatites, *J. Inorg. Nucl. Chem.* 40 (1978) 15–21.
- [8] P. Ducheyne, S. Radin, M. Heughebaert, J.C. Heughebaert, Calcium phosphate ceramic coatings on porous titanium: effect of structure and composition on electrophoretic deposition, vacuum sintering and in vitro dissolution, *Biomaterials* 11 (1990) 244–254.
- [9] J. Weng, X. Liu, X. Zhang, X. Ji, Thermal decomposition of hydroxyapatite structure induced by titanium and its dioxide, *J. Mater. Sci. Lett.* 13 (1994) 159–161.
- [10] W. Rathje, Zur Kenntnis der Phosphate. I. Über Hydroxyapatite, *Bodenk. Pflernach.* 12 (1939) 121–128.
- [11] E. Hayek, H. Newsely, Pentacalcium monohydroxyorthophosphate (hydroxyapatite), *Inorg. Synth.* 7 (1963) 63–65.
- [12] H. Monma, T. Kamiya, Preparation of hydroxyapatite by the hydrolysis of brushite, *J. Mater. Sci.* 22 (1987) 4247–4250.
- [13] E. Hayer, J. Lechleitner, W. Bohler, Hydrothermalsynthese von hydroxyapatite, *Angew. Chim.* 67 (1955) 326.
- [14] O.R. Trautz, X-ray diffraction of biological and synthetic apatites, *Ann. N. Y. Acad. Sci.* 60 (1955) 696–712.
- [15] K. Hosoi, T. Hashida, H. Tkahashi, N. Yamasaki, T. Korenaga, New processing technique for hydroxyapatite ceramics by the hydrothermal hot-pressing method, *J. Am. Ceram. Soc.* 79 (1996) 2771–2774.
- [16] M. Jarcho, C.H. Bolen, M.B. Thomas, J. Bobick, J.F. Kay, R.H. Doremus, Hydroxyapatite synthesis and characterization in dense polycrystalline form, *J. Mater. Sci.* 11 (1976) 2027–2035.
- [17] I.A. Blench, Electromigration in thin aluminum films on titanium nitride, *J. Appl. Phys.* 47 (1976) 1203–1208.

## Selenium Distribution in Human Soft Tissue Determined by Using X-ray Scanning Analytical Microscope and X-ray Absorption Fine Structure Analysis

Motohiro Uo,<sup>\*1</sup> Kiyotaka Asakura,<sup>2</sup> Takao Kohgo,<sup>3</sup> and Fumio Watari<sup>1</sup>

<sup>1</sup>Department of Biomedical Materials and Engineering, Graduate School of Dental Medicine, Hokkaido University, North 13, West 7, Kita-ku, Sapporo 060-8586

<sup>2</sup>Catalyst Research Center, Hokkaido University, North 21, West 10, Kita-ku, Sapporo 001-0021

<sup>3</sup>Department of Oral Pathology, Graduate School of Dental Medicine, Hokkaido University, North 13, West 7, Kita-ku, Sapporo 060-8586

(Received October 5, 2005; CL-051270; E-mail: uo@den.hokudai.ac.jp)

Se localization in the human oral mucosae which contain dental amalgam or dental silver alloy particles was analyzed by X-ray scanning analytical microscopy (XSAM). Se distribution was visualized, and the localization in the neighbor of amalgam or silver particles was confirmed. The chemical state of Se was analyzed by X-ray absorption fine structure (XAFS) analysis. Se was estimated as the low valency state. The possibility of using XSAM and XAFS for the analysis of the distribution and chemical state of rarely contained elements in biological tissue was suggested.

Selenium (Se) is an essential element in humans. It is important not only as a cofactor in enzymes but also in detoxification of heavy metals such as mercury. The relationship between the level of Se and heavy metals, especially mercury (Hg) and silver, had been studied.<sup>1</sup> A positive correlation between Se and Hg in blood was reported. As the detoxification mechanism, the formation of Hg-selenoprotein complex was suggested. However, the current study of the interaction of Se and heavy metals employed macroscopic analysis. The distribution of Se in the areas surrounding heavy metals in the human body has not yet been studied, because the concentration of Se in human body is very low, making it difficult to measure the elemental distribution.

The authors employed the X-ray scanning analytical microscopy (XSAM) for the analysis of metallic elements in soft and hard tissues.<sup>2</sup> XSAM enables elemental distribution analysis from Na to U by energy-dispersive spectroscopy of fluorescent X-rays in air without pretreatment even if the sample contains water. This feature is desirable for the analysis of biological specimens. XSAM also has higher sensitivity for heavier elements than elemental distribution analysis with electron microscopic methods. The authors also employed the X-ray absorption fine structure (XAFS) analysis for human tissue containing metallic elements in low concentrations. XAFS analysis using synchrotron radiation makes it possible to analyze the state of eroded metal in the human body at low concentrations of around 1 to 100 ppm by using fluorescence XAFS.<sup>3</sup> In this study, XSAM and fluorescence XAFS were employed to determine the selenium distribution in the human oral mucosa containing metallic dental restoratives.

Two oral mucosa specimens excised from two different patients, which contained particle-like foreign bodies, were subjected to XSAM and XAFS analyses. These specimens were excised for pathological diagnosis for pigmentation. The speci-

mens were fixed in 10% neutral buffered formalin and embedded in paraffin by the conventional method. The embedded tissue blocks were sliced. The residual blocks of tissue embedded in paraffin were subjected to elemental distribution analysis using XSAM (XGT-2000V, Horiba Co., Ltd., Kyoto, Japan). The XSAM observation was carried with the incident X-rays generated from an Rh anode under conditions of 50 kV and 1 mA. The incident X-ray was passed through the X-ray guide tube (XGT) 100  $\mu\text{m}$  in diameter. During the XSAM observation, the specimen stage was scanned in the air. The mapping images were integrated 100 times (scan speed was 3000 seconds per scan).

The XAFS spectra were measured at BL-9A of the Photon Factory, Institute of Material Structure Science, High-Energy Accelerator Organization (KEK-PF). The electron storage ring was operated at 2.5 GeV with 300–500 mA. The synchrotron radiation was monochromatized with an Si(111) double-crystal monochromator. The incident X-ray was focused using two bent conical mirrors into 1 mm in diameter and the specified area of the specimen where Se was enriched was irradiated. The XAFS spectra of the Se K-edge were measured in a fluorescent mode using a multielement solid-state detector (Camberra).  $I_0$  signals were monitored using an  $\text{N}_2$  filled ionization chamber.

Figure 1 shows the transmission X-ray image and S, Hg, Ag, and Se distribution images of specimen A with XSAM. The S distribution image shows the shapes of specimens. In the transmission X-ray image, spotlike untransparent parts were found. In these untransparent spots, Hg and Ag were observed. Se existed in the vicinity of the Hg and Ag localized spots. Usually, Se

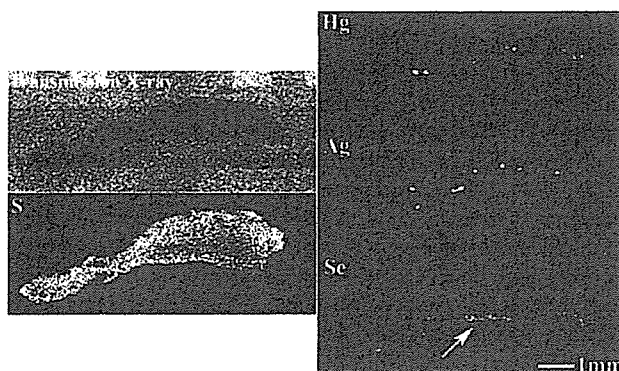


**Figure 1.** Elemental distribution images of dental amalgam-like particles in human oral mucosa (specimen A).



is not detected in the tissue by XSAM image because of its low concentration. Therefore, Se localization would be caused by the existence of Hg and Ag. Dental amalgam consists of Ag–Sn–Cu alloy powder and mercury. The foreign bodies in specimen A were considered to be dental amalgam. After trituration of the alloy powder and mercury, the mixture is applied in the oral cavity. In the initial stage of trituration, there are large amounts of unreacted mercury and alloy powder, and the mixture shows little fluidity. The mechanical strength of the dental amalgam in the initial state is low. After 24 to 48 h of trituration, most of the mercury is amalgamated. In Figure 1, Ag and Hg show different distributions. This suggests that the debris of dental amalgam formed in the filling or polishing process in the earlier stage was dispersed into the oral mucosa. Selenium was concentrated in the tissue surrounding the dispersed foreign bodies.

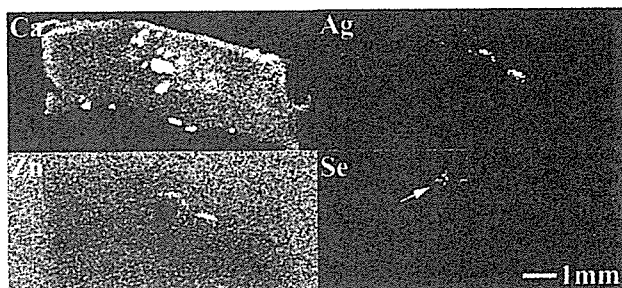


**Figure 2.** Elemental distribution images of dental silver alloy-like particles in human oral mucosa (specimen B).

Figure 2 shows the Ca, Zn, Ag, and Se distribution images of specimen B obtained by XSAM. Ca localization caused by the calcification was observed. Ag and Zn were localized in the same positions. This means the foreign body consists of homogeneous materials such as alloys. In the fluorescent X-ray spectrum from the particle indicated by the arrow in Figure 2, Ag, Zn, and Cu were detected. These are typical components of dental silver alloy. Se was localized in the vicinity of the silver alloy particles, but the Se concentration was lower than that of specimen A. In Figures 1 and 2, the Se was localized in the vicinity of Hg or Ag, but their distributions were not same. The reason of the difference in the distribution was assumed as follows. The XSAM images mainly show the distribution of alloy particles, which were encapsulated by granulation tissue. The Se would be reacted with the dissolved Hg or Ag outside of the granulation tissue, the Se distribution would be differ from those of Hg or Ag.

The parts indicated by arrows in the Se distribution images in Figures 1 and 2 were measured with the fluorescence XAFS method. The Se K-edge XANES spectra of the above specimens and those of Se compounds are shown in Figure 3. Yamamoto et al. reported that the absorption edge of Se shifts toward higher energy with the increase of valence.<sup>4</sup> The absorption edges of the spectra of specimens A and B were slightly shifted to higher energy than that of metallic Se, and there is shoulder structure at 12.66 keV in both specimen A and B. This suggests that the Se in those specimens would be mostly in the low-valence state

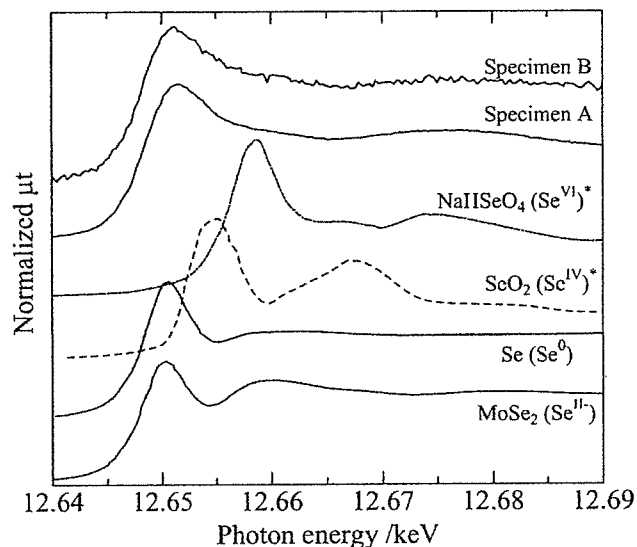


**Figure 3.** The Se K-edge XAFS spectra of oral mucosa specimens A and B and standard specimens (\* after Yamamoto et al.<sup>4</sup>).

(nearly zero) and there would be some variety in the valency of Se.

Previously, the relationship between the Se and Hg concentrations in blood was reported.<sup>1</sup> The detoxification of Hg by selenoprotein was suggested as a possible reason of this phenomenon. In this study, the localization in the vicinity of dental amalgam which contained Hg and Ag and dental silver alloy was clearly visualized using XSAM and their chemical states were estimated using XAFS. Areas with high concentrations of Se were observed within 1 mm from the amalgam or silver alloy particles. Thus, the Se localization towards the Hg and Ag was revealed.

The XAFS measurements were done with the approval of the Photon Factory Advisory Committee (Proposal No. 2004G084). Part of this study was supported by Northern Advancement Center for Science and Technology, Japan.

#### References

- 1 M. Molin, B. Bergman, S. L. Marklund, A. Schütz, S. Skerfving, *Acta Odontol. Scand.* **1990**, *48*, 189; E. Johansson, *J. Trace Elem. Electrolytes Health Dis.* **1991**, *5*, 273; M. Kauppi, *Heavy Met. Bull.* **1995**, *2*, 16; G. Drasch, S. Mailänder, C. Schlosser, G. Roeder, *J. Trace Elem. Med. Biol.* **2003**, *17*, 165.
- 2 M. Uo, F. Watari, A. Yokoyama, H. Matsuno, T. Kawasaki, *J. Biomed. Mater. Res. Part B: Appl. Biomater.* **2004**, *70B*, 146.
- 3 M. Uo, K. Asakura, A. Yokoyama, K. Tamura, Y. Totsuka, T. Akasaka, F. Watari, *Chem. Lett.* **2005**, *34*, 776.
- 4 T. Yamamoto, S. Itoh, Y. Tochiyama, N. Noda, H. Akiho, M. Kobayashi, S. Noguchi, *Yokosuka Research Report*, **2004**, Vol. W03034, p. 1.

## Effect of Surface Condition of Dental Zirconia Ceramic (Denzir) on Bonding

Motohiro UO<sup>1</sup>, Göran SJÖGREN<sup>2</sup>, Anders SUNDH<sup>3</sup>, Mitsunari GOTO<sup>1</sup>, Fumio WATARI<sup>1</sup>  
and Maud BERGMAN<sup>2</sup><sup>1</sup>Department of Biomedical Materials and Engineering, Graduate School of Dentistry, Hokkaido University, 060-8586, Sapporo, Japan<sup>2</sup>Department of Dental Materials Science, Faculty of Medicine, Umeå University, SE-901 87 Umeå, Sweden<sup>3</sup>Cad.esthetics AB, SE-931 27 Skellefteå, Sweden and National Dental Health Service, County Council of Västerbotten, SE-935 32 Norsjö, Sweden

Corresponding author, Motohiro Uo E-mail:uo@den.hokudai.ac.jp

Received June 13, 2006/Accepted July 30, 2006

Yttria partially stabilized zirconia (YPSZ) ceramics are suitable for dental and medical use because of their high fracture toughness and chemical durability. The purpose of this study was to examine the bonding behavior of a dental YPSZ ceramic, Denzir. After being subjected to various surface treatments, Denzir specimens were bonded to each other using an adhesive resin composite, glass ionomer, or zinc phosphate cement. Bonding strength was then determined by the shearing test. No significant differences ( $p > 0.05$ ) were observed between SiC- and Al<sub>2</sub>O<sub>3</sub>-blasted specimens. In all surface treatments, the shear bond strength significantly ( $p < 0.05$ ) increased in the order of adhesive resin composite cement > glass ionomer cement > zinc phosphate cement. Moreover, silanization with methacryloxy propyl trimethoxysilane slightly increased the bonding strength of the adhesive resin composite cement.

Key words: Bonding strength, Surface treatment

## INTRODUCTION

In recent years, the demand for dental restorations with more esthetic and biocompatible properties has increased. As a result, various ceramics have been widely studied and applied as dental materials<sup>1–6</sup>. In particular, yttria partially stabilized zirconia (YPSZ) is a ceramic that exhibits superior fracture toughness and chemical durability compared to other ceramics<sup>1,2</sup>. Due to these advantageous properties, YPSZ has been extensively employed for medical and dental uses<sup>2–5</sup>.

However, manufacturing of dental restorations requires complicated machining of various shapes and dimensions – and it is difficult to achieve accurate machining. Through recent advances in the CAD/CAM technique, YPSZ ceramics can now be employed for complicated dental restorations such as inlays, copings, and fixed partial denture (FPD) frameworks<sup>6–10</sup>. Dental restorations using YPSZ can be made by milling enlarged restorations out of homogenous ceramic green-body blanks of zirconia, which are then sintered and shrunken to the desired final dimensions<sup>7</sup>. Alternatively, restorations can be milled directly with the final dimensions out of high-density, sintered, prefabricated YPSZ blanks – known as hot isostatically pressed (HIPed) zirconia blanks<sup>6,8–10</sup>.

In an earlier report, the authors investigated the cytotoxicity and bonding property of HIPed YPSZ<sup>11</sup>. In that study<sup>11</sup>, HIPed YPSZ showed no cytotoxicity and exhibited high bonding to glass ionomer cement,

but relatively low bonding strength to adhesive resin composite cement<sup>11</sup>. Kern and Wegner, however, reported that a durable bond to YPSZ was achieved by using a phosphate monomer-containing resin composite bonding cement<sup>12</sup>. In their study<sup>12</sup>, as in most of the earlier studies evaluating the bond strength of various luting agents to YPSZ ceramics<sup>13–19</sup>, specimens were made out of homogenous ceramic green-body zirconia.

Since HIPed YPSZ blanks have been successfully employed in the fabrication of dental all-ceramic crowns and FPDs<sup>8–10</sup>, the bonding properties of this type of zirconia ceramic present an interest. However, in a survey of the published literature, only one article<sup>11</sup> was found that addressed the bonding properties of HIPed YPSZ. The purpose of this study, therefore, was to evaluate the bonding properties of various bonding cements to HIPed YPSZ and the effects of surface roughness and pretreatment on bonding strength.

## MATERIALS AND METHODS

*Preparation of HIPed YPSZ specimens*

Twenty HIPed YPSZ (Denzir, Cad.esthetics AB, Skellefteå, Sweden) specimens were machined into a rectangular shape (14 mm × 14 mm × 5 mm) using the Cad.esthetics CAD/CAM system (Cad.esthetics AB). Some specimens were then sandblasted with 70- $\mu$ m Al<sub>2</sub>O<sub>3</sub> (Hi-Alumina, Shofu, Kyoto, Japan) and the remainder with 125- $\mu$ m SiC powder (Carborundum, Shofu, Kyoto, Japan) – all with 0.3 MPa for 30

seconds at a distance of 10 mm.

Thereafter, SiC-blasted specimens were etched with a phosphoric acid gel (K-etchant gel, Kuraray, Kurashiki, Japan) for 10 seconds. In addition, the etched specimens intended to be cemented with an adhesive resin composite cement were silanized in one of the following ways: (i) treatment with Clearfil Porcelain Bond Activator (Kuraray, Kurashiki, Japan) mixed with Clearfil Linerbond IIS (Kuraray, Kurashiki, Japan) for 10 seconds in accordance with the manufacturer's instructions; or (ii) heating with 10% methacryloxy propyl trimethoxysilane (MPTS, Tokyo Kasei Kogyo, Tokyo, Japan)-toluene (dehydrated) solution at 60°C for one hour, followed by drying in a vacuum.

*Bonding procedure*

Cements used for the bonding test were: (i) a zinc phosphate cement (Elite Cement, GC, Tokyo, Japan); (ii) a glass ionomer cement (Fuji I, GC, Tokyo, Japan); and (iii) an adhesive resin composite cement (Panavia 21, Kuraray, Kurashiki, Japan). Using one of the abovementioned cements, the surface-treated specimens were bonded to corresponding specimens with a similar surface condition. The bonding area was 14 mm×5 mm. Bonded specimens were then stored at 37°C, 100% RH for one hour. Seven replicates were prepared for each condition. The abbreviations of surface treatments and cements are given in Table 1.

*Surface roughness and bond strength measurements*

Surface profile and mean surface roughness (Ra) were determined using a surface profilometer (Surfcom 2000, Tokyo Seimitsu Co. Ltd., Tokyo, Japan).

Bonding strength was determined by the shearing test method using a universal testing machine (Model 4204, Instron, Canton, USA). Apparatus for the shear test is shown in Fig. 1. Shear force was applied at a crosshead speed of 0.5 mm/sec. Results of the shear test were then analyzed statistically using ANOVA and Scheffé's test at a significance level of  $p < 0.05$ . After the bonding test, YPSZ blocks were polished with emery paper (#80) until the attached cement layer was removed. Then, the polished

blocks were surface-treated again and used for the next bonding test.

*SEM and EDX analyses*

After the shear test, the fractured surfaces were analyzed using a scanning electron microscope (SEM) (S-2380, Hitachi, Tokyo, Japan). Then, with an energy-dispersed X-ray detector (EDX) (Genesis, EDAX Japan, Tokyo, Japan), the elemental distribution image of the observed surface was acquired.

RESULTS

*Mean surface roughness*

Fig. 2 shows the surface profiles and mean surface roughness levels (Ra) of Al<sub>2</sub>O<sub>3</sub>-blasted and SiC-blasted *cum* phosphoric acid-etched YPSZ specimens. The SiC-blasted surface had a clearly rougher profile than the Al<sub>2</sub>O<sub>3</sub>-blasted surface. Mean surface roughness (Ra) of the SiC-blasted surface was 0.86 μm, twice that of the Al<sub>2</sub>O<sub>3</sub>-blasted surface (0.43 μm).

*Shear bond strength*

Shear bonding strengths of Al<sub>2</sub>O<sub>3</sub>-blasted and SiC-blasted *cum* phosphoric acid-etched YPSZ specimens luted with the three types of cement are shown in Fig. 3. In all surface treatments, the shear bond strength increased in the order of adhesive resin

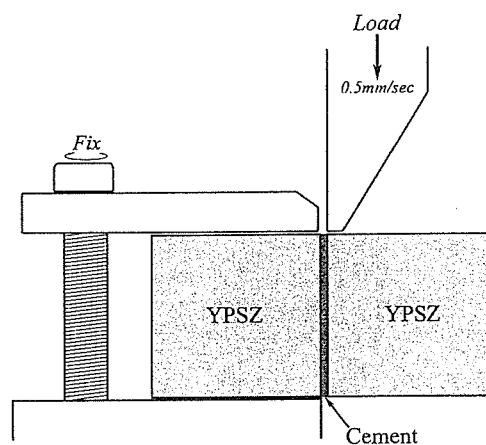


Fig. 1 Apparatus for the shear bond test.

Table 1 Abbreviations for surface treatments and cements

Abbreviation	Cement or surface treatment
ZP	Zinc phosphate cement
GI	Glass ionomer cement
AR	Adhesive resin composite cement
AB	Al <sub>2</sub> O <sub>3</sub> -blasted
SB	SiC-blasted
PE	Phosphate gel-treated
PBA	Treated with Clearfil Porcelain Bond Activator
MPTA	Treated with 10% methacryloxy propyl trimethoxysilane-toluene solution

composite cement > glass ionomer cement > zinc phosphate cement. Among the three cement types, the bonding strength differed significantly ( $p < 0.05$ ). Between the  $Al_2O_3$ - and SiC-blasted YPSZ specimens, there were no significant differences ( $p > 0.05$ ) in shear bond strength. Thus, bonding strength depended on the cement type, since neither surface roughness significantly affected the bonding

strength.

Fig. 4 shows the effects on the bonding strength of surface treatment using phosphoric acid, PBA, or MPTS in combination with the various cements. Statistical significance of the bond strengths of SiC-blasted specimens is shown in Table 2. In all surface treatments, the shear bond strength increased in the order of adhesive resin composite cement > glass ionomer cement > zinc phosphate cement. With the adhesive resin cement, the MPTS treatment yielded the highest bonding strength but their difference was of low significance ( $0.1 > p > 0.05$ ).

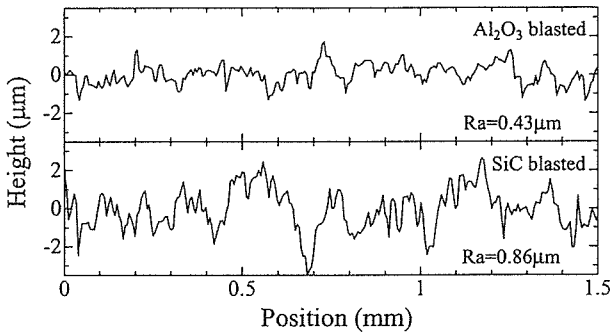


Fig. 2 Surface profiles and mean surface roughness (Ra) levels of YPSZ specimens blasted with  $Al_2O_3$  or SiC.

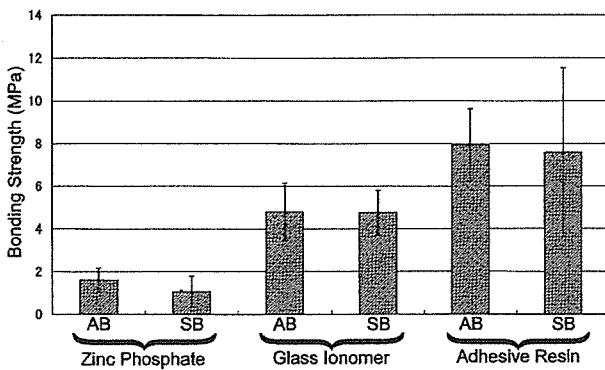


Fig. 3 Shear bond strengths of  $Al_2O_3$ -blasted and SiC-blasted *cum* phosphoric acid-etched YPSZ specimens in combination with the three cements studied.

SEM and EDX observations

Fig. 5 shows the SEM and elemental distribution images of the fracture surfaces bonded with zinc phosphate, glass ionomer, and adhesive resin composite cements. The surfaces of the zinc phosphate-

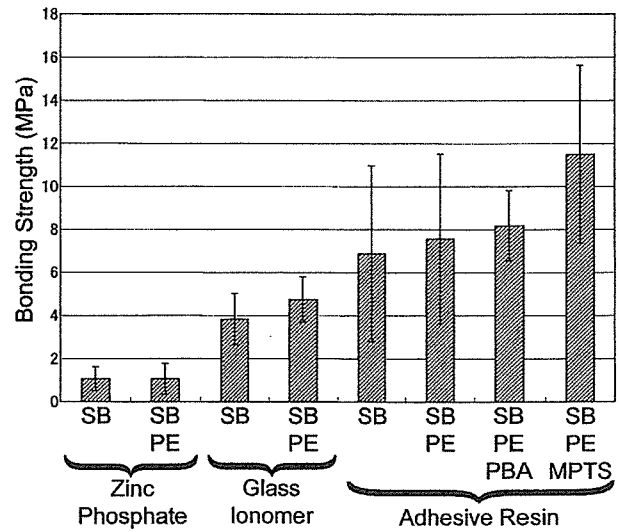


Fig. 4 Effect on the bonding strength to SiC-blasted and phosphoric acid-etched YPSZ specimens of various surface treatments in combination with the three cements studied.

Table 2 Summary of the statistical analysis of the bond strengths of SiC-blasted specimens. Results of ANOVA supplemented with Scheffé's test (n.s.: no significant differences; \*:  $p < 0.05$ ; \*\*:  $p < 0.001$ ).

Cement		ZP		GI		AR			
Cement	Surface treatment	SB	SB PE	SB	SB PE	SB	SB PE	SE PE PBS	SB PE MPTS
ZP	SB SB-PE	n.s.							
GI	SB SB-PE	**	**			n.s.			
AR	SB	*	*	n.s.	n.s.				
	SB-PE	*	*	*	n.s.	n.s.			
	SB-PE-PBA	**	**	**	**	n.s.	n.s.		
	SB-PE-MPTS	**	**	**	*	n.s.	n.s.	n.s.	